

Exact Multimode Quantization of Superconducting Circuits via Boundary Admittance

Mustafa Bakr^{1,*} and Robin Wopalenski¹

¹*Clarendon Laboratory, Department of Physics, University of Oxford*

We show that the Schur complement of the nodal admittance matrix, which reduces a multi-port electromagnetic environment to the driving-point admittance $Y_{\text{in}}(s)$ at the Josephson junction, naturally leads to an eigenvalue-dependent boundary condition determining the dressed mode spectrum. This identification provides a four-step quantization procedure: (i) compute or measure $Y_{\text{in}}(s)$, (ii) solve the boundary condition $sY_{\text{in}}(s) + 1/L_J = 0$ for dressed frequencies, (iii) synthesize an equivalent passive network, (iv) quantize with the full cosine nonlinearity retained. Within passive lumped-element circuit theory, we prove that junction participation decays as, we prove that junction participation decays as $O(\omega_n^{-1})$ at high frequencies when the junction port has finite shunt capacitance, ensuring ultraviolet convergence of perturbative sums without imposed cutoffs. The standard circuit QED parameters, coupling strength g , anharmonicity α , and dispersive shift χ , emerge as controlled limits with explicit validity conditions.

I. INTRODUCTION

A Josephson junction [1] embedded in an electromagnetic environment experiences that environment as a frequency-dependent load. At low frequencies, the surrounding circuit appears predominantly inductive; at high frequencies, predominantly capacitive; and near resonances, strongly reactive. The starting point of this paper is that this entire influence can be compressed into a single scalar object that fully determines the junction's linear response: the driving-point admittance seen at the junction port, $Y_{\text{in}}(\omega)$. Once $Y_{\text{in}}(\omega)$ is known, either from measurement or from electromagnetic simulation followed by network reduction, it can be used to construct a quantitative quantum description of the coupled system.

The picture is simple. Consider a junction shunted by its capacitance C_J and connected to an otherwise arbitrary passive linear network built from resonators, transmission lines, and coupling elements. When the junction oscillates at angular frequency ω , it injects current into the network, and the ratio of current to voltage at the port is $Y_{\text{in}}(\omega)$. This back-action reshapes the junction dynamics. Near an environmental resonance, the admittance is large and the junction hybridizes strongly with the resonant structure into dressed normal modes. Far from resonances, the junction behaves as a weakly perturbed anharmonic oscillator with small admixtures of environmental degrees of freedom. A crucial consequence is that the high-frequency sector is not only benign but naturally suppressed. For $\omega \gg \omega_p$ where ω_p is the junction plasma frequency [2], the shunt capacitance presents a low impedance that effectively short-circuits the junction port. In this regime, environmental eigenfunctions have vanishing junction participation: the junction node becomes energetically expensive to excite, suppressing high-frequency mode amplitudes at

the junction. This physical suppression provides an intrinsic ultraviolet regularization within passive lumped-element circuit theory following directly from circuit elements present in any realistic device. This ultraviolet decoupling is consistent with exact multimode quantization analyses of superconducting circuits, where treating the electromagnetic environment as a passive infinite-dimensional system yields finite Hamiltonians without ad-hoc cutoffs [3]. Closely related ultraviolet-convergent treatments of capacitive coupling to infinite-dimensional circuits were developed earlier in Refs. [4, 5].

The framework developed here begins from $Y_{\text{in}}(\omega)$ and proceeds to an exact circuit Hamiltonian that retains the full cosine nonlinearity of the Josephson potential. From this Hamiltonian one obtains the dressed spectrum, including avoided crossings and level repulsion [6, 7]. The familiar circuit-QED parameters, qubit-mode coupling strengths [8, 9], transmon anharmonicity [2], and dispersive shifts [10, 11], emerge as controlled limits in appropriate parameter regimes. Because the construction retains the full cosine potential without invoking the rotating-wave approximation [12, 13], corrections beyond the RWA and dispersive limits are obtained by systematic expansion of the exact Hamiltonian. Dissipative rates follow from combining the admittance description with Fermi's golden rule [14, 15], recovering the Purcell effect [16] and its multimode generalizations [17, 18]. The central mathematical result is that the Schur complement reduction, which eliminates internal degrees of freedom to yield the driving-point admittance, constructs an eigenvalue-dependent boundary condition in the sense of Sturm-Liouville spectral theory. This equivalence, made explicit in Theorem III.2, provides both conceptual clarity and practical computational tools: the dressed mode frequencies are roots of the boundary condition equation $sY_{\text{in}}(s) + 1/L_J = 0$, and the mode shapes follow from network synthesis of the positive-real function $Y_{\text{in}}(s)$.

The practical advantage of this approach is that circuit parameters are not treated as fit variables. They are inferred from the environment as encoded in $Y_{\text{in}}(\omega)$, so

* mustafa.bakr@physics.ox.ac.uk

that the quantum description remains anchored to the measured or simulated electromagnetic structure while avoiding the computational burden of full field quantization. The Schur complement, a classical tool in linear algebra for block Gaussian elimination [19, 20], has found widespread application in computational electromagnetics. In microwave engineering, the coupled-integral-equation technique uses Schur complement reductions to analyze waveguide discontinuities and multiport junctions [21, 22]. Similar reduction procedures appear in domain decomposition methods for scattering problems [23] and in iterative solvers for coupled electromagnetic-circuit problems [24]. The same mathematical structure underlies circuit quantization: the driving-point admittance obtained by eliminating internal nodes simultaneously encodes the boundary condition for dressed modes.

The first demonstration of coherent control of a superconducting qubit was achieved in a single-Cooper-pair box measured via quasiparticle tunneling [25]. The theoretical description of superconducting quantum circuits is often introduced through the Jaynes–Cummings Hamiltonian [6] and its dispersive limit [2, 8, 13]. The transmon qubit design [2] and the circuit-QED architecture [9, 26] have become the dominant paradigm for superconducting quantum computing. Impedance-based quantization methods [3, 27–33] provide a more systematic foundation by tying the quantum model directly to a measured or simulated linear response function. The present work is motivated by three points where the standard treatment remains either implicit or incomplete. In particular, multiport impedance quantization [28, 29, 34–36] establishes that broad classes of positive-real impedance matrices can be synthesized and quantized to yield an exact Hamiltonian. Our contribution is not the existence of impedance-synthesis quantization per se, but a boundary-condition formulation that makes the dressed-mode structure, ultraviolet behavior, and multi-mode interference directly computable from $Y_{\text{in}}(s)$ with explicit convergence guarantees.

First, the reduction of a multiport electromagnetic environment to a single-port admittance at the junction is typically presented as an engineering convenience. Here we show that the Schur-complement reduction constructs an eigenvalue-dependent boundary condition at the junction node. In that language, the dressed linear mode condition,

$$s Y_{\text{in}}(s) + \frac{1}{L_J} = 0, \quad (1)$$

is not merely a root-finding recipe but the spectral condition imposed by the junction termination. This connection to Sturm–Liouville theory [37–39], developed further in [43], provides a clean conceptual bridge between circuit reduction and operator-theoretic mode structure. Early studies focused on affine and single-pole eigenparameter dependence at the boundary [37, 38]. The general rational case, under Nevan-

linna–Herglotz restrictions, was developed in detail by Binding, Browne, and Watson [40, 41] and by Dijkstra, Langer, and de Snoo [42].

Second, multimode treatments are frequently accompanied by ultraviolet worries: naive perturbative sums over modes appear to diverge unless an external cutoff is imposed. The resolution is that junction participation decays at high frequency in any circuit with finite shunt capacitance. We show that when Y_{in} includes a finite shunt capacitance at the junction port, a condition satisfied by physical realization within passive lumped-element circuit theory, the junction participation scales as $\phi_n^J = O(\omega_n^{-1})$ for large mode frequency ω_n . This yields $\lambda_n \propto \omega_n^{-3/2}$ for the zero-point flux participation and implies absolute convergence of the perturbative sums that generate Kerr terms [27], Lamb shifts [44, 45], dispersive shifts [10], and related quantities. The result is stated and proved at the theorem level within the assumptions of lumped passive circuit theory [46, 47].

Third, the usual derivations of the coupling g [8], anharmonicity $\alpha = -E_C/\hbar$ [2], and dispersive shift $\chi = g^2\alpha/[\Delta(\Delta + \alpha)]$ [2, 11] are often developed inside the Jaynes–Cummings framework [6] and only then interpreted in circuit terms. We reverse this logic. Starting from the exact Hamiltonian

$$\hat{H} = \sum_n \hbar\omega_n \hat{a}_n^\dagger \hat{a}_n - E_J \cos\left(\frac{\hat{\Phi}_J}{\varphi_0}\right), \quad (2)$$

we expand the cosine in a controlled way and recover the standard formulas as limits of the exact circuit model. This non-circular route makes clear which approximations are invoked, where they enter, and how they can be relaxed systematically. The operator-level content of parameters such as g is thereby made explicit: g is the coefficient of the bilinear operator $(\hat{b} + \hat{b}^\dagger)(\hat{a} + \hat{a}^\dagger)$ in the cosine expansion, and the rotating-wave approximation projects this onto the excitation-exchange sector $\hat{a}^\dagger \hat{b} + \hat{a} \hat{b}^\dagger$. The validity of this projection requires conditions we state precisely.

The paper is organized to follow the quantization pipeline illustrated in Fig. 1: from the measured or simulated admittance, through network reduction and synthesis, to the quantized Hamiltonian and physical observables. Section II establishes circuit variables and Josephson constitutive relations [1, 48], with particular attention to the convention that Y_{in} includes the junction capacitance C_J . Section III derives the Schur complement reduction and proves its equivalence to an eigenvalue-dependent boundary condition (Theorem III.2). Section IV treats network synthesis in Foster and Brune canonical forms [49–51], including lossy networks. Section V carries out canonical quantization [31, 48] to obtain the exact multimode Hamiltonian with the full cosine nonlinearity retained. Section VI proves the ultraviolet convergence theorem with explicit assumptions (Theorem VI.4). Section VII analyzes multi-mode interference and Purcell suppression directly from the boundary-condition admittance. Sec-

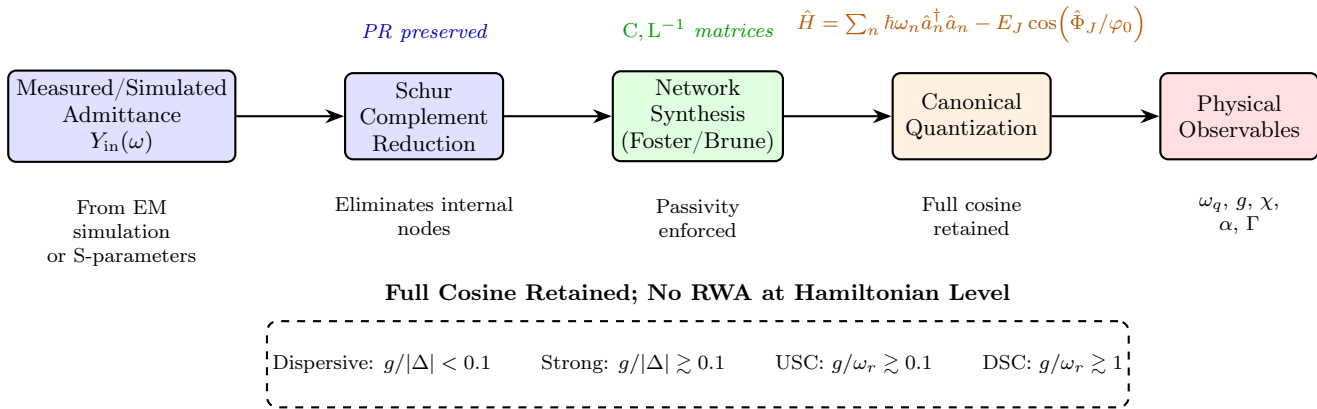


FIG. 1. Overview of the boundary condition framework. The measured or simulated admittance $Y_{\text{in}}(\omega)$ is reduced to the junction port via Schur complement, synthesized into an equivalent circuit, and quantized to yield the exact Hamiltonian. Physical observables are extracted by numerical diagonalization or perturbative expansion. The Hamiltonian retains the full cosine nonlinearity; standard circuit QED emerges as the dispersive limit. The dashed box indicates that the framework applies uniformly from dispersive through deep strong coupling, different regimes are distinguished by which terms in the cosine expansion are numerically significant, not by modifications to the quantization procedure.

tion VIII delineates coupling regimes with explicit validity conditions, and Section IX derives the standard circuit-QED formulas as controlled limits. Section X provides a complete design example.

II. CIRCUIT VARIABLES AND CONSTITUTIVE RELATIONS

The quantum description of electrical circuits requires dynamical variables that admit a Lagrangian formulation and subsequent canonical quantization. The natural choice is the node flux, a time-integrated voltage that serves as the generalized coordinate for circuit dynamics. This section establishes the node flux formalism, derives the constitutive relations for linear and nonlinear elements, and states the convention for treating the junction capacitance that is maintained throughout.

A. The Node Flux as Generalized Coordinate

Consider a circuit network with N nodes, where one node is designated as the ground reference with zero potential. The node flux at node i is defined as

$$\Phi_i(t) \equiv \int_{-\infty}^t V_i(t') dt', \quad (3)$$

where $V_i(t)$ is the voltage at node i relative to ground. This definition implies the voltage-flux relation

$$V_i(t) = \dot{\Phi}_i(t), \quad (4)$$

and in the Laplace domain with zero initial conditions,

$$\tilde{V}_i(s) = s\tilde{\Phi}_i(s). \quad (5)$$

The node flux has dimensions of magnetic flux (Weber = Volt·second). This is not coincidental: by Faraday's law, the time-integrated voltage around a closed loop equals the magnetic flux threading the loop. For superconducting circuits, the node flux is directly related to the gauge-invariant phase difference across circuit elements, with the conversion factor being the reduced flux quantum $\varphi_0 = \Phi_0/(2\pi)$.

The physical interpretation becomes concrete when we consider how the flux appears in the energy expressions. For a capacitor, the stored energy depends on voltage, hence on $\dot{\Phi}$, making capacitance play the role of mass in the mechanical analogy. For an inductor, the stored energy depends on current, which is proportional to $\dot{\Phi}$ itself, making inductance play the role of a spring constant. This identification of capacitance with kinetic energy and inductance with potential energy is the foundation of the Lagrangian formulation.

B. Constitutive Relations for Linear Elements

The current through a capacitor with capacitance C is proportional to the rate of change of voltage:

$$I_C = C \frac{dV}{dt} = C\ddot{\Phi}. \quad (6)$$

The energy stored in the capacitor is

$$U_C = \frac{1}{2}CV^2 = \frac{1}{2}C\dot{\Phi}^2, \quad (7)$$

which depends on $\dot{\Phi}$ and therefore contributes to the kinetic energy in the Lagrangian.

The current through an inductor with inductance L is given by integrating the voltage:

$$I_L = \frac{1}{L} \int V dt = \frac{\Phi}{L}. \quad (8)$$

Note the absence of time derivatives: the inductor current equals the flux divided by inductance, a relation that holds instantaneously in the time domain. In the Laplace domain, $\tilde{I}_L(s) = \tilde{\Phi}(s)/L$, with no factor of s in the denominator.

The energy stored in the inductor is

$$U_L = \frac{1}{2}LI_L^2 = \frac{\Phi^2}{2L}, \quad (9)$$

which depends on Φ alone and contributes to the potential energy.

A resistor with resistance R dissipates energy and cannot be directly incorporated into a conservative Lagrangian. Its current is

$$I_R = \frac{V}{R} = \frac{\dot{\Phi}}{R}. \quad (10)$$

The treatment of dissipation requires coupling to a bath of oscillators, which we address in Section IV.

C. The Josephson Junction: Constitutive Relations

The Josephson junction is characterized by two fundamental relations discovered by Josephson in 1962 [1]. The first Josephson relation gives the supercurrent through the junction as a function of the superconducting phase difference φ across the barrier:

$$I_J = I_c \sin \varphi, \quad (11)$$

where I_c is the critical current. The second Josephson relation connects the voltage across the junction to the time derivative of the phase:

$$V_J = \varphi_0 \frac{d\varphi}{dt}, \quad \text{where} \quad \varphi_0 \equiv \frac{\hbar}{2e} = \frac{\Phi_0}{2\pi}. \quad (12)$$

Integrating the second relation gives $\varphi = \Phi_J/\varphi_0$, where Φ_J is the flux across the junction. The current-flux relation becomes

$$I_J = I_c \sin \left(\frac{\Phi_J}{\varphi_0} \right). \quad (13)$$

The potential energy is obtained by computing the work done against the junction current:

$$U_J = \int I_J d\Phi_J = -I_c \varphi_0 \cos \left(\frac{\Phi_J}{\varphi_0} \right) = -E_J \cos \left(\frac{\Phi_J}{\varphi_0} \right), \quad (14)$$

where $E_J \equiv I_c \varphi_0 = \hbar I_c / (2e)$ is the Josephson energy. We have chosen the constant of integration so that $U_J(\Phi_J = 0) = -E_J$, the minimum of the potential.

The cosine potential has minima at $\Phi_J = 2\pi n \varphi_0$ for integer n . Near any minimum, the potential is approximately harmonic:

$$U_J \approx -E_J + \frac{E_J}{2\varphi_0^2} \Phi_J^2 = -E_J + \frac{\Phi_J^2}{2L_J}, \quad (15)$$

where the Josephson inductance is

$$L_J \equiv \frac{\varphi_0^2}{E_J} = \frac{\varphi_0}{I_c}. \quad (16)$$

This linearization is valid for $|\Phi_J| \ll \varphi_0$, or equivalently $|\varphi| \ll 1$. In the transmon regime where $E_J/E_C \gg 1$, the phase fluctuations are small and the linearization provides a good starting point, though the exact treatment retains the full cosine.

D. The Junction Capacitance Convention

A physical Josephson junction has a geometric capacitance C_J arising from the parallel-plate structure of the electrodes separated by the insulating barrier. This capacitance participates in the circuit dynamics and must be accounted for in the quantization. However, there is freedom in how to incorporate C_J : it can be included in the linear electromagnetic environment described by Y_{in} , or it can be treated as a separate term in the junction Hamiltonian with a charging energy $Q_J^2/(2C_J)$.

Assumption II.1 (Junction Capacitance Inclusion). *The driving-point admittance $Y_{\text{in}}(s)$ seen by the junction includes the junction capacitance C_J . Under this convention, the linear electromagnetic environment encompasses all linear elements connected to the junction node, including C_J . The Josephson junction then contributes only the nonlinear cosine potential to the Hamiltonian:*

$$H_J = -E_J \cos \left(\frac{\hat{\Phi}_J}{\varphi_0} \right). \quad (17)$$

No separate charging energy term $Q_J^2/(2C_J)$ appears.

This convention has three important consequences that justify its adoption. First, it avoids double-counting: if C_J were included both in Y_{in} and as a separate charging term, the junction capacitance would be counted twice, leading to incorrect eigenfrequencies. Second, it ensures that the junction flux Φ_J is a coordinate within the synthesized network with a well-defined conjugate momentum. When C_J is part of the network, the momentum $Q_J = \partial \mathcal{L} / \partial \dot{\Phi}_J$ arises naturally from the Lagrangian formulation, with Q_J representing the charge on the total capacitance connected to the junction node. Third, it simplifies the boundary condition equation: the condition $sY_{\text{in}}(s) + 1/L_J = 0$ for the dressed mode frequencies involves only the admittance and the Josephson inductance, with no additional terms.

The alternative convention, excluding C_J from Y_{in} and adding a charging term, is mathematically valid if handled consistently. However, mixing elements of both conventions leads to double-counting. We maintain Assumption II.1 throughout this paper.

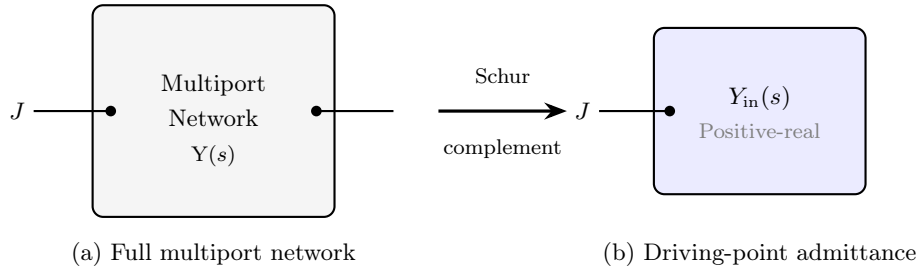


FIG. 2. Schur complement reduction. (a) A multiport network with junction port J and internal nodes \bar{J} (gray dots). (b) The Schur complement eliminates internal nodes, yielding the scalar driving-point admittance $Y_{\text{in}}(s)$ at the junction. The positive-real property is preserved under this reduction.

E. High-Frequency Behavior of the Admittance

An important consequence of including C_J in Y_{in} is a constraint on the high-frequency behavior:

$$Y_{\text{in}}(i\omega) = i\omega C_{\Sigma} + O(1) \quad \text{as } \omega \rightarrow \infty, \quad (18)$$

where $C_{\Sigma} \geq C_J > 0$ is the total shunt capacitance at the junction node. This behavior reflects the physical fact that at high frequencies, the capacitive admittance dominates over inductive or resistive contributions.

The condition $C_{\Sigma} > 0$ is essential for the ultraviolet convergence proved in Section VI. It ensures that the junction is not connected to a purely inductive environment, which would lead to divergent zero-point fluctuations. For any physical circuit containing a Josephson junction with finite $C_J > 0$, Assumption II.1 automatically guarantees Eq. (18).

III. THE SCHUR COMPLEMENT AS BOUNDARY CONDITION

The central mathematical operation in reducing a multiport electromagnetic environment to a single-port description is the Schur complement. In this section, we derive the Schur complement formula and prove that it yields precisely the frequency-dependent boundary condition at the junction node. This equivalence connects standard circuit reduction (Schur complement) to eigenparameter-dependent boundary conditions in the sense of Sturm–Liouville theory [39–42]. We developed the boundary-condition viewpoint for dispersive readout in a transmon–resonator setting in [43]; here we show the same structure arises generally from the driving-point admittance $Y_{\text{in}}(s)$ and use it as the basis for exact multimode quantization.

A. Multiport Admittance and the Schur Complement

Consider a linear electromagnetic network with N ports, characterized by an admittance matrix $Y(s)$ re-

lating port currents to port voltages in the Laplace domain:

$$I(s) = Y(s) \cdot V(s). \quad (19)$$

We partition the ports into two groups: the junction port J , and all remaining ports collectively denoted \bar{J} . The admittance matrix takes the block form

$$Y(s) = \begin{pmatrix} Y_{JJ}(s) & Y_{J\bar{J}}(s) \\ Y_{\bar{J}J}(s) & Y_{\bar{J}\bar{J}}(s) \end{pmatrix}, \quad (20)$$

where Y_{JJ} is the self-admittance at port J , $Y_{J\bar{J}}$ is a row vector of transfer admittances from ports \bar{J} to port J , $Y_{\bar{J}J}$ is a column vector of transfer admittances from port J to ports \bar{J} , and $Y_{\bar{J}\bar{J}}$ is the admittance matrix among the remaining ports.

The constitutive relation for the full network is

$$\begin{pmatrix} I_J \\ I_{\bar{J}} \end{pmatrix} = \begin{pmatrix} Y_{JJ} & Y_{J\bar{J}} \\ Y_{\bar{J}J} & Y_{\bar{J}\bar{J}} \end{pmatrix} \begin{pmatrix} V_J \\ V_{\bar{J}} \end{pmatrix}. \quad (21)$$

Now suppose the ports \bar{J} are internal nodes of the network with no external current injection. This constraint is expressed by setting $I_{\bar{J}} = 0$, which from the second block row of Eq. (21) gives

$$0 = Y_{\bar{J}J}(s)V_J + Y_{\bar{J}\bar{J}}(s)V_{\bar{J}}. \quad (22)$$

Solving for the internal voltages yields

$$V_{\bar{J}} = -Y_{\bar{J}\bar{J}}^{-1}(s)Y_{\bar{J}J}(s)V_J. \quad (23)$$

Substituting into the first block row gives

$$\begin{aligned} I_J &= Y_{JJ}V_J + Y_{J\bar{J}}V_{\bar{J}} \\ &= Y_{JJ}V_J - Y_{J\bar{J}}Y_{\bar{J}\bar{J}}^{-1}Y_{\bar{J}J}V_J \\ &= [Y_{JJ} - Y_{J\bar{J}}Y_{\bar{J}\bar{J}}^{-1}Y_{\bar{J}J}]V_J. \end{aligned} \quad (24)$$

The quantity in brackets is the Schur complement of $Y_{\bar{J}\bar{J}}$ in Y :

$$Y_{\text{in}}(s) = Y_{JJ}(s) - Y_{J\bar{J}}(s)Y_{\bar{J}\bar{J}}^{-1}(s)Y_{\bar{J}J}(s). \quad (25)$$

This formula has a direct physical interpretation. The first term Y_{JJ} is the self-admittance at port J with

all other ports open-circuited. The second term accounts for the current that flows from port J through the network to the other ports, induces voltages there according to the internal admittance matrix, and returns to port J through the transfer admittances. The Schur complement thus represents the effective admittance seen by an observer at port J when all other ports are internal to the network with no external excitation.

Figure 2 illustrates this reduction schematically: the multiport network with internal nodes is reduced to a single driving-point admittance at the junction port. The key insight is that no information relevant to the junction dynamics is lost in this reduction; the entire influence of the electromagnetic environment on the junction is encoded in the scalar function $Y_{\text{in}}(s)$.

B. Positive-Real Preservation

The Schur complement preserves the positive-real property, which is essential for physical realizability of the reduced network.

Proposition III.1 (Positive-Real Preservation). *If the admittance matrix $Y(s)$ is positive-real, representing a passive network, then the Schur complement $Y_{\text{in}}(s)$ is also positive-real.*

Proof. A matrix-valued function $Y(s)$ is positive-real if it satisfies three conditions: analyticity in the open right half-plane $\text{Re}(s) > 0$, the reality condition $Y(s^*) = Y^*(s)$, and the positive semidefiniteness condition $Y(s) + Y^\dagger(s) \geq 0$ for $\text{Re}(s) > 0$.

For the Schur complement, analyticity in the right half-plane follows from analyticity of all component matrices and the fact that $Y_{\bar{J}\bar{J}}(s)$ is invertible for $\text{Re}(s) > 0$ when $Y(s)$ is positive-real (since positive-real matrices have positive-definite real parts in the right half-plane). The reality condition is inherited directly from the block components.

For positive semidefiniteness, we use the characterization of Schur complements for positive semidefinite matrices. When $Y(s) + Y^\dagger(s) \geq 0$, the matrix can be written in block form with the $(1, 1)$ block being $Y_{JJ} + Y_{JJ}^*$ and the $(2, 2)$ block being $Y_{\bar{J}\bar{J}} + Y_{\bar{J}\bar{J}}^\dagger$. By the theory of Schur complements for Hermitian matrices [19], if the full matrix is positive semidefinite and the $(2, 2)$ block is positive definite, then the Schur complement of the $(2, 2)$ block satisfies the same semidefiniteness. Applying this to $Y(s) + Y^\dagger(s)$ yields

$$Y_{\text{in}}(s) + Y_{\text{in}}^*(s) \geq 0 \quad (26)$$

for $\text{Re}(s) > 0$, completing the proof. \square

This result is physically essential: it guarantees that $Y_{\text{in}}(s)$ represents a realizable passive network regardless of the complexity of the original multiport structure. The subsequent network synthesis procedure can therefore construct an equivalent lumped-element circuit.

C. Connection to the Boundary Condition

We now establish the central result of this section: the Schur complement reduction produces the frequency-dependent boundary condition at the junction node. This connection reveals that circuit reduction and spectral theory are two perspectives on the same mathematical structure.

Consider the junction node in the synthesized circuit. Kirchhoff's current law states that the sum of currents entering the node must vanish. The current from the linear electromagnetic environment, flowing through the admittance Y_{in} , is related to the junction voltage by

$$I_{\text{env}}(t) = \mathcal{L}^{-1} \left[Y_{\text{in}}(s) \tilde{V}_J(s) \right], \quad (27)$$

where \mathcal{L}^{-1} denotes the inverse Laplace transform. In the Laplace domain, using the voltage-flux relation $V_J = s\Phi_J$, this becomes

$$\tilde{I}_{\text{env}}(s) = Y_{\text{in}}(s) \tilde{V}_J(s) = s Y_{\text{in}}(s) \tilde{\Phi}_J(s). \quad (28)$$

The current through the Josephson junction is determined by the first Josephson relation. Under our convention that C_J is included in Y_{in} , the junction contributes only the supercurrent:

$$I_J(t) = I_c \sin \left(\frac{\Phi_J(t)}{\varphi_0} \right). \quad (29)$$

Kirchhoff's current law at the junction node requires

$$I_{\text{env}}(t) + I_J(t) = 0. \quad (30)$$

For the linear normal modes of the system, we seek solutions where the junction flux oscillates harmonically: $\Phi_J(t) = \phi_n^J e^{i\omega_n t}$ with small amplitude $|\phi_n^J| \ll \varphi_0$. In this regime, the Josephson current can be linearized as $\sin(\Phi_J/\varphi_0) \approx \Phi_J/\varphi_0$, giving $I_J \approx \Phi_J/L_J$ where $L_J = \varphi_0/I_c = \varphi_0^2/E_J$ is the Josephson inductance. Taking the Laplace transform of the linearized Kirchhoff equation yields

$$s Y_{\text{in}}(s) \tilde{\Phi}_J(s) + \frac{\tilde{\Phi}_J(s)}{L_J} = 0. \quad (31)$$

For nontrivial solutions with $\tilde{\Phi}_J \neq 0$, the frequency must satisfy the boundary condition equation

$$s Y_{\text{in}}(s) + \frac{1}{L_J} = 0. \quad (32)$$

Theorem III.2 (Boundary Condition Equivalence). *Let $Y(s)$ be the nodal admittance matrix of a passive linear network, and let $Y_{\text{in}}(s)$ be the Schur complement obtained by eliminating all nodes except a designated port node J . If a Josephson junction with inductance $L_J = \varphi_0^2/E_J$ terminates this port, then the linearized dressed mode frequencies ω_n of the coupled system are the positive solutions of*

$$s Y_{\text{in}}(s) + \frac{1}{L_J} = 0 \quad \text{at } s = i\omega_n. \quad (33)$$

This equation is the spectral condition imposed by the junction termination, with $Y_{\text{in}}(s)$ encoding the frequency-dependent boundary data.

The boundary condition (32) has a natural interpretation in Sturm-Liouville theory. For a differential operator on an interval with a boundary condition that depends on the eigenvalue parameter, the eigenvalues are determined by a transcendental equation involving the boundary data. Here, the “boundary” is the junction node, and the “eigenvalue-dependent boundary condition” is precisely Eq. (32), where the admittance $Y_{\text{in}}(s)$ encodes how the electromagnetic environment responds at frequency s . This connection to Sturm-Liouville theory with eigenparameter-dependent boundary conditions [37, 38] provides powerful analytical tools for understanding the mode structure, including completeness of the eigenfunction expansion and the asymptotic distribution of eigenvalues.

Remark III.3 (Equivalence to Transmission Line Boundary Condition). *In Ref. [43], the boundary condition at a transmon terminating a transmission line resonator was derived from the wave equation via the variational principle. The result was a condition of the form $\phi'(L)/\phi(L) = F(\lambda)$, where $F(\lambda)$ is a rational function of the spectral parameter $\lambda = \omega^2/v^2$ with poles associated with the junction’s effective linear response. The present derivation shows that $F(\lambda)$ is directly related to Y_{in} : the Schur complement reduction and the Sturm-Liouville boundary condition are two perspectives on the same mathematical object. This equivalence provides a bridge between the circuit-theoretic and field-theoretic approaches to quantization.*

D. Graphical Solution and Mode Structure

The boundary condition equation (32) can be solved graphically by plotting the left-hand side as a function of frequency along the imaginary axis $s = i\omega$. Writing $Y_{\text{in}}(i\omega) = G(\omega) + iB(\omega)$ where $G(\omega) \geq 0$ is the conductance and $B(\omega)$ is the susceptance, the boundary condition becomes

$$i\omega[G(\omega) + iB(\omega)] + \frac{1}{L_J} = 0, \quad (34)$$

which separates into real and imaginary parts:

$$\text{Real: } -\omega B(\omega) + \frac{1}{L_J} = 0, \quad (35)$$

$$\text{Imaginary: } \omega G(\omega) = 0. \quad (36)$$

For a lossless network where $G(\omega) = 0$ identically, the imaginary equation is automatically satisfied, and the mode frequencies are determined by the real equation alone:

$$\omega B(\omega) = \frac{1}{L_J}. \quad (37)$$

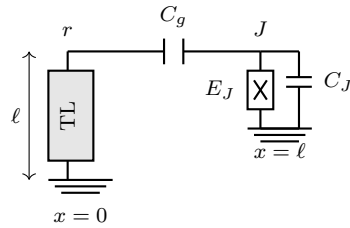


FIG. 3. Quarter-wave transmission line resonator coupled to a transmon qubit. The resonator is shorted at $x = 0$ and couples through capacitance C_g to the transmon at $x = \ell$. The transmon consists of a Josephson junction with energy E_J shunted by capacitance C_J .

Figure 4 illustrates this graphical solution for a transmon coupled to a resonator. The blue curve shows the dimensionless product $\omega L_J B(\omega)$ as a function of frequency normalized to the bare resonator frequency. Mode frequencies occur where this curve intersects unity. The susceptance $B(\omega)$ diverges at the bare resonator frequencies, creating vertical asymptotes that partition the frequency axis into intervals. Between consecutive asymptotes, the product $\omega L_J B(\omega)$ varies continuously from $+\infty$ to $-\infty$ (or vice versa), guaranteeing exactly one zero crossing per interval by the intermediate value theorem. This topological argument ensures that the number of dressed modes equals the number of poles in the admittance plus one (for the junction mode).

Near an avoided crossing where the bare qubit frequency $\omega_p = 1/\sqrt{L_J C_\Sigma}$ approaches a bare resonator frequency ω_r , the two solutions repel each other. The minimum separation at the avoided crossing equals the vacuum Rabi splitting $2g$, providing a direct connection between the boundary condition roots and the coupling strength. This geometric picture shows that the dressed modes are genuine hybridized states whose character changes continuously as parameters are varied, not perturbative corrections to bare modes.

E. Illustrative Example: Quarter-Wave Resonator

To make the abstract formulas concrete, consider a quarter-wave coplanar waveguide resonator of length ℓ , shorted at $x = 0$ and coupled through a capacitance C_g to a transmon at $x = \ell$. The transmon has junction capacitance C_J and Josephson inductance L_J . Figure 3 shows the circuit topology.

We define two ports: port r at the resonator end of the coupling capacitor and port J at the junction node. The transmission line resonator, when terminated in a short at $x = 0$, presents an input admittance at $x = \ell$ given by

$$Y_r(s) = \frac{1}{Z_0} \coth\left(\frac{s\ell}{v}\right), \quad (38)$$

where $Z_0 = \sqrt{L_\ell/C_\ell}$ is the characteristic impedance,

$v = 1/\sqrt{L_\ell C_\ell}$ is the phase velocity, and L_ℓ , C_ℓ are the inductance and capacitance per unit length. On the imaginary axis $s = i\omega$, this becomes $Y_r(i\omega) = (i/Z_0) \cot(\omega\ell/v)$, which is purely imaginary (reactive) and has poles at the bare resonator frequencies $\omega_n^{(0)} = (2n-1)\pi v/(2\ell)$ for $n = 1, 2, 3, \dots$

The two-port admittance matrix is constructed from Kirchhoff's laws at each node. At the resonator node, the current entering from the transmission line plus the current through the coupling capacitor must sum to zero for an internal node:

$$I_r = Y_r V_r + sC_g(V_r - V_J) = (Y_r + sC_g)V_r - sC_g V_J. \quad (39)$$

At the junction node, including C_J per our convention:

$$I_J = sC_J V_J + sC_g(V_J - V_r) = -sC_g V_r + s(C_g + C_J)V_J. \quad (40)$$

The resulting admittance matrix is

$$Y(s) = \begin{pmatrix} Y_r + sC_g & -sC_g \\ -sC_g & s(C_g + C_J) \end{pmatrix}. \quad (41)$$

Applying the Schur complement formula (25) with the junction as port J and the resonator as port \bar{J} :

$$\begin{aligned} Y_{\text{in}}(s) &= s(C_g + C_J) - \frac{(-sC_g)(-sC_g)}{Y_r + sC_g} \\ &= s(C_g + C_J) - \frac{s^2 C_g^2}{Y_r + sC_g} \\ &= sC_J + \frac{sC_g Y_r}{Y_r + sC_g}. \end{aligned} \quad (42)$$

This result has transparent physical content. The first term sC_J is the admittance of the junction capacitance to ground, confirming that C_J is included in Y_{in} per our convention. The second term is the resonator admittance Y_r as modified by the series coupling capacitor C_g . In the limit $sC_g \ll Y_r$ near resonance, this term reduces to sC_g , showing that the junction sees primarily the coupling capacitor. In the limit $sC_g \gg Y_r$ far from resonance, it approaches Y_r , showing that strong coupling transfers the full resonator admittance. The Schur complement formula thus automatically captures the frequency-dependent nature of the coupling. Figure 4 illustrates the graphical solution of Eq. (43), showing how the dressed mode frequencies emerge as intersections.

The boundary condition equation (32) for this system reads

$$s \left[sC_J + \frac{sC_g Y_r(s)}{Y_r(s) + sC_g} \right] + \frac{1}{L_J} = 0. \quad (43)$$

Substituting the cotangent form of the resonator admittance and evaluating on the imaginary axis $s = i\omega$ yields a transcendental equation whose roots give the dressed mode frequencies. Near the fundamental resonator frequency $\omega_1^{(0)} = \pi v/(2\ell)$, two solutions emerge: a

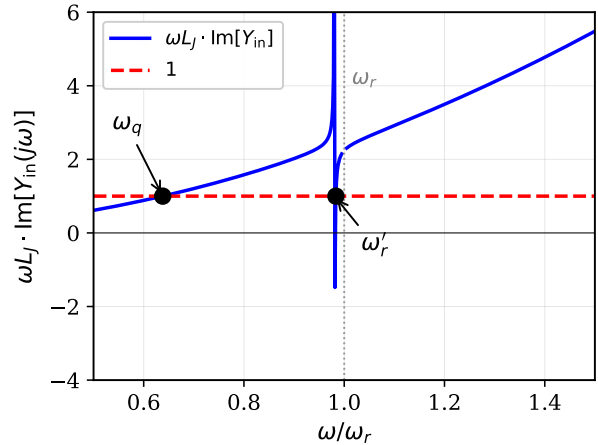


FIG. 4. Graphical solution of the boundary condition equation $sY_{\text{in}}(s) + 1/L_J = 0$. The blue curve shows the dimensionless product $\omega L_J \cdot \text{Im}[Y_{\text{in}}(j\omega)]$ as a function of frequency normalized to the bare resonator frequency ω_r . Dressed mode frequencies occur where this curve intersects unity (red dashed line). For a transmon capacitively coupled to a resonator, two solutions emerge: the qubit mode ω_q at lower frequency and the dressed resonator mode ω'_r pushed slightly below the bare resonator frequency. The vertical asymptote at ω_r reflects the pole in the resonator admittance. Circuit parameters: $E_J/h = 12$ GHz, $C_J = 85$ fF, resonator at 7 GHz with $C_r = 200$ fF, and coupling capacitance $C_g = 8$ fF.

lower-frequency qubit-like mode and a higher-frequency resonator-like mode, exhibiting an avoided crossing as the bare qubit frequency is tuned through the resonator. The vacuum Rabi splitting at the avoided crossing, obtained from the minimum separation of the roots, provides the coupling strength g directly from the boundary condition analysis.

IV. NETWORK SYNTHESIS

Given the driving-point admittance $Y_{\text{in}}(s)$, the next step is to construct an equivalent lumped-element circuit whose input admittance equals this function. This circuit represents the *linear electromagnetic environment* seen by the junction; the Josephson nonlinearity is not part of the synthesis and will be reintroduced only during quantization (Section V). This inverse problem, known as network synthesis, provides the physical degrees of freedom that will be quantized. The key result, due to Brune [50], is that any positive-real function admits such a realization. This section treats Foster synthesis for lossless networks and Brune synthesis for the general lossy case, followed by the analysis of complex poles and mode linewidths.

A. Foster Synthesis for Lossless Networks

For lossless (purely reactive) networks, the admittance is purely imaginary on the real frequency axis: $Y_{\text{in}}(i\omega) = iB(\omega)$, where $B(\omega)$ is the susceptance. The positive-real conditions for such functions have strong implications: the poles of $Y_{\text{in}}(s)$ must lie on the imaginary axis at complex-conjugate pairs $s = \pm i\omega_k$, each pole must be simple (first-order), and the residues at poles on the positive imaginary axis must be real and positive.

These properties follow from the physical requirement that the network stores but does not dissipate energy. A pole at $s = i\omega_k$ represents a resonance where the susceptance diverges, corresponding to a series LC circuit tuned to frequency ω_k . The positivity of residues ensures that energy stored in the resonance is positive, as required by passivity.

The Foster canonical form [49] expresses any lossless positive-real driving-point admittance as a partial fraction expansion:

$$Y(s) = sC_\infty + \frac{1}{sL_0} + \sum_{k=1}^N \frac{sC_k\omega_k^2}{s^2 + \omega_k^2}. \quad (44)$$

The term sC_∞ represents a shunt capacitance to ground, present when the admittance grows without bound as $s \rightarrow \infty$. The term $1/(sL_0)$ represents an inductor to ground, present when the admittance has a pole at $s = 0$ (dc). Each term in the summation represents a series LC branch resonating at angular frequency $\omega_k = 1/\sqrt{L_k C_k}$.

The circuit parameters are extracted from the residues of $Y(s)$. At a pole $s = i\omega_k$, the residue is computed as

$$\begin{aligned} \text{Res}[Y(s), i\omega_k] &= \lim_{s \rightarrow i\omega_k} (s - i\omega_k)Y(s) \\ &= \lim_{s \rightarrow i\omega_k} (s - i\omega_k) \frac{sC_k\omega_k^2}{s^2 + \omega_k^2}. \end{aligned} \quad (45)$$

Using the factorization $s^2 + \omega_k^2 = (s - i\omega_k)(s + i\omega_k)$, this becomes

$$\text{Res}[Y(s), i\omega_k] = \frac{i\omega_k \cdot C_k\omega_k^2}{2i\omega_k} = \frac{C_k\omega_k^2}{2}. \quad (46)$$

Inverting this relation gives the branch capacitance and inductance:

$$C_k = \frac{2|\text{Res}[Y(s), i\omega_k]|}{\omega_k^2}, \quad L_k = \frac{1}{\omega_k^2 C_k}. \quad (47)$$

The physical interpretation of the Foster form, illustrated in Fig. 5, is that the admittance decomposes into parallel branches, each resonating at a distinct frequency. At frequency ω_k , the k -th series LC branch presents zero impedance (infinite admittance), acting as a short circuit that dominates the response. Far from ω_k , the branch contributes capacitively when $\omega < \omega_k$

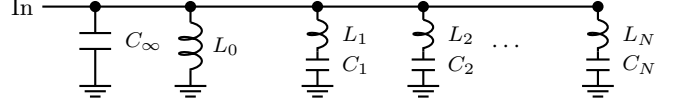


FIG. 5. Foster canonical form for a lossless positive-real admittance. The circuit consists of parallel branches connected to a common input node: a direct capacitor C_∞ to ground capturing the high-frequency asymptotic behavior, an inductor L_0 to ground present when there is a pole at dc, and series LC tanks tuned to the resonant frequencies $\omega_k = 1/\sqrt{L_k C_k}$. Each tank represents an environmental mode that can exchange energy with the junction.

or inductively when $\omega > \omega_k$, with diminishing influence as the detuning increases. Each branch represents an environmental mode that can exchange energy with the junction, and the branch parameters determine both the mode frequency and its coupling strength to the junction.

B. Positive-Real Fitting and Passivity Enforcement

In practice, $Y_{\text{in}}(s)$ is obtained from electromagnetic simulation or network analyzer measurement, providing values at a discrete set of frequencies. Before synthesis can proceed, the admittance must be fitted to a rational function. Vector fitting [52] is the standard algorithm for this task, producing a fit of the form

$$Y_{\text{fit}}(s) = d + se + \sum_{k=1}^N \frac{r_k}{s - p_k}, \quad (48)$$

where d and e are real constants representing the dc conductance and high-frequency capacitance, the poles p_k lie in the left half-plane for stable systems or on the imaginary axis for lossless approximations, and the residues r_k may be complex for complex-conjugate pole pairs.

A critical subtlety is that vector fitting does not automatically enforce positive-realness. The fitting algorithm minimizes a least-squares error between the rational function and the data, but this optimization may produce a result that violates passivity. Specifically, the fitted admittance may have $\text{Re}[Y_{\text{fit}}(i\omega)] < 0$ for some frequencies, corresponding to negative conductance. Such a function cannot represent a passive physical network, and attempting to synthesize it would produce circuits with negative resistances. More seriously for quantum applications, quantizing such a circuit yields a Hamiltonian that is unbounded from below, leading to unphysical spectra and dynamics.

The passivity condition requires

$$G_{\text{fit}}(\omega) \equiv \text{Re}[Y_{\text{fit}}(i\omega)] \geq 0 \quad \text{for all real } \omega. \quad (49)$$

When vector fitting violates this condition, passivity enforcement must be applied before synthesis. Several approaches exist: residue perturbation methods adjust the

residues r_k minimally to restore passivity; Hamiltonian perturbation methods modify the state-space representation; and convex optimization methods find the closest passive system in an appropriate norm [53]. The choice of method affects the accuracy of the enforced fit, and care must be taken to ensure that the passivity enforcement does not significantly degrade the match to the original data in frequency regions important for the quantum dynamics.

The number of poles N in the fit determines the number of modes in the quantized system. Increasing N improves the fit accuracy, capturing finer features of the admittance, but increases the computational cost of subsequent calculations. The ultraviolet convergence theorem (Section VI) ensures that physical observables converge as N increases, so truncation at finite N introduces controlled error. In practice, including modes up to several times the plasma frequency $\omega_p = 1/\sqrt{L_J C_\Sigma}$ captures the relevant physics while maintaining computational tractability.

C. Brune Synthesis for Lossy Networks

When the network contains dissipative elements, the admittance $Y_{\text{in}}(s)$ is no longer purely imaginary on the frequency axis. The positive-real property generalizes to require that $Y_{\text{in}}(s)$ be analytic for $\text{Re}(s) > 0$ and satisfy $\text{Re}[Y_{\text{in}}(s)] \geq 0$ in the right half-plane. On the imaginary axis, we decompose the admittance into its real and imaginary parts as $Y_{\text{in}}(i\omega) = G(\omega) + iB(\omega)$, where the conductance $G(\omega) \geq 0$ represents dissipation and the susceptance $B(\omega)$ represents reactive energy storage.

The Brune synthesis algorithm [50] provides a systematic procedure for realizing any positive-real function as a lumped network containing resistors, inductors, capacitors, and ideal transformers. This synthesis step is essential: it guarantees that the reduced admittance obtained from the boundary-condition formulation corresponds to a physical passive circuit and therefore admits a canonical quantization. The synthesized network contains only the linear electromagnetic environment; the Josephson nonlinearity is reintroduced only after synthesis is complete, ensuring clean separation between the passive linear structure and the nonlinear junction potential. The algorithm is iterative, reducing the complexity of the admittance at each stage by extracting a Brune section until only a resistive remainder is left.

The first step in each iteration identifies the frequency ω_0 where the conductance $G(\omega) = \text{Re}[Y_{\text{in}}(i\omega)]$ attains its minimum value $G_0 \geq 0$. For a positive-real function, this minimum exists and is non-negative by the passivity requirement. When $G_0 > 0$ at a finite frequency $0 < \omega_0 < \infty$, the full Brune cycle applies. When $G_0 = 0$, the function has a transmission zero at ω_0 where the network is purely reactive, allowing simplified extraction procedures.

For the case $G_0 > 0$, the second step extracts a

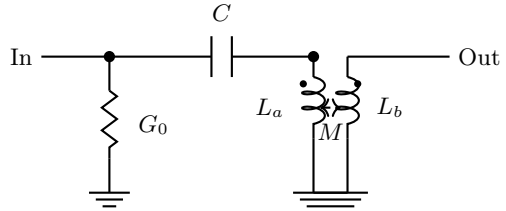


FIG. 6. Brune section for positive-real synthesis. The shunt conductance G_0 represents the minimum loss at the critical frequency. The series capacitor C and mutually coupled inductors L_a , L_b with mutual inductance M form the reactive portion that extracts the transmission zero at ω_0 . The dots indicate the polarity of the mutual coupling.

shunt conductance G_0 from the admittance by defining $Y_1(s) = Y_{\text{in}}(s) - G_0$. The remainder $Y_1(s)$ remains positive-real since we subtracted the global minimum of the real part, and it satisfies $\text{Re}[Y_1(i\omega_0)] = 0$, meaning $Y_1(i\omega_0)$ is purely imaginary.

The third step extracts the susceptance at the critical frequency. Define $B_0 = \text{Im}[Y_1(i\omega_0)]$ and form $Y_2(s) = Y_1(s) - sB_0/\omega_0$. For $B_0 > 0$, this corresponds to extracting a capacitor $C_0 = B_0/\omega_0$; for $B_0 < 0$, an inductor $L_0 = -\omega_0/B_0$. The remainder satisfies $Y_2(i\omega_0) = 0$, so ω_0 is now a zero of $Y_2(s)$.

The fourth step analyzes the impedance near this transmission zero. Since $Y_2(i\omega_0) = 0$, the impedance $Z_2(s) = 1/Y_2(s)$ has a pole at $s = i\omega_0$. Near this pole, we can write

$$Z_2(s) = \frac{\alpha}{s - i\omega_0} + Z_{\text{reg}}(s), \quad (50)$$

where α is the residue and $Z_{\text{reg}}(s)$ is the regular (analytic) part. For $Z_2(s)$ to be positive-real, the residue α at a purely imaginary pole must be real and positive.

The Brune section, shown in Fig. 6, is a two-port network that extracts this pole while maintaining positive-realness of the remainder. It consists of a series capacitor C and two mutually coupled inductors L_a and L_b with mutual inductance M . The impedance matrix of the Brune section is

$$Z_{\text{Brune}}(s) = \begin{pmatrix} \frac{1}{sC} + sL_a & -sM \\ sM & -sL_b \end{pmatrix}, \quad (51)$$

where the sign pattern in the off-diagonal terms reflects the current direction conventions, and the input impedance when the output is terminated by impedance Z_L is

$$Z_{\text{in}}(s) = \frac{1}{sC} + sL_a - \frac{s^2 M^2}{-sL_b + Z_L}. \quad (52)$$

The element values are determined by three conditions. First, the series LC combination must resonate at the critical frequency: $\omega_0^2 = 1/(L_a C)$. Second, the residue of the pole at $s = i\omega_0$ must match α from

Eq. (50). Third, the mutual inductance must satisfy the realizability constraint $|M| \leq \sqrt{L_a L_b}$. Solving these conditions with the symmetric choice $L_b = L_a$ yields

$$C = \frac{1}{2\alpha\omega_0}, \quad L_a = L_b = \frac{2\alpha}{\omega_0}, \quad M = \frac{2\alpha}{\omega_0}. \quad (53)$$

The equality $M = L_a = L_b$ corresponds to perfect coupling $k = M/\sqrt{L_a L_b} = 1$, meaning the coupled inductors can be replaced by an ideal transformer. This limiting case is the minimum-capacitance solution; choosing smaller C gives $k < 1$ and imperfect coupling.

After extracting the Brune section, the remainder impedance $Z_3(s)$ has McMillan degree reduced by two, corresponding to removal of one complex-conjugate pole pair. The algorithm iterates, returning to the first step with the new admittance $Y_3(s) = 1/Z_3(s)$, until the remainder is a constant real number $R_\infty \geq 0$ representing a pure terminating resistance. The complete synthesized network consists of a cascade of Brune sections, each contributing a shunt conductance, a series capacitor, and coupled inductors, terminated by the final resistance.

When ideal transformers appear in the synthesized network, they impose algebraic constraints rather than differential equations. The flux variables on either side of a 1:1 transformer are identified (up to sign), reducing the number of independent degrees of freedom. During quantization, these constraints must be handled through symplectic reduction, identifying the physical coordinates that remain after constraint elimination. This procedure is essential for obtaining the correct mode count and canonical commutation relations in the quantized theory.

D. Complex Poles and Mode Linewidths

In the lossless limit where $G(\omega) \equiv 0$, the poles of the system response lie on the imaginary axis at $s = \pm i\omega_n$, corresponding to undamped oscillations. When dissipation is introduced through finite conductance, these poles migrate into the left half-plane, acquiring finite lifetimes. This subsection derives the relationship between the admittance structure and the mode decay rates, establishing the connection between circuit parameters and the quality factors of the dressed modes.

Consider the boundary condition equation (32) written as

$$F(s) \equiv sY_{\text{in}}(s) + \frac{1}{L_J} = 0. \quad (54)$$

In the lossless case with $Y_{\text{in}}(s) = iB(s/i)$ purely imaginary on the imaginary axis, the solutions $s_n^{(0)} = i\omega_n^{(0)}$ are purely imaginary. When dissipation is introduced and $Y_{\text{in}}(s)$ acquires a positive real part, the poles shift to

$$s_n = -\frac{\kappa_n}{2} + i\omega_n, \quad (55)$$

where $\kappa_n > 0$ is the energy decay rate (the full width at half maximum of the spectral line in angular frequency units) and ω_n is the shifted oscillation frequency.

To derive the decay rate perturbatively, we expand $F(s)$ around the lossless pole. Writing the admittance as $Y_{\text{in}}(s) = iB(s) + G(s)$ where B is the susceptance (imaginary part on the imaginary axis) and G is the conductance (real part), and treating G as a small perturbation, the boundary function becomes $F(s) = F_0(s) + sG(s)$ where $F_0(s) = isB(s) + 1/L_J$ is the lossless boundary function.

At the lossless pole $s_n^{(0)} = i\omega_n^{(0)}$, we have $F_0(s_n^{(0)}) = 0$ by definition. The perturbed pole $s_n = s_n^{(0)} + \delta s$ satisfies $F(s_n) = 0$. Expanding to first order in both δs and G :

$$0 = F_0(s_n^{(0)}) + \delta s \cdot F_0'(s_n^{(0)}) + s_n^{(0)}G(s_n^{(0)}) + O(G^2, \delta s \cdot G). \quad (56)$$

Since $F_0(s_n^{(0)}) = 0$, solving for δs gives

$$\delta s = -\frac{s_n^{(0)}G(\omega_n^{(0)})}{F_0'(s_n^{(0)})}, \quad (57)$$

where $G(\omega_n^{(0)}) = G(i\omega_n^{(0)})$ is the conductance evaluated at the lossless mode frequency.

The derivative of the lossless boundary function at $s = i\omega$ is

$$F_0'(i\omega) = iB(\omega) + i\omega \cdot i \frac{dB}{d\omega} = iB(\omega) - \omega \frac{dB}{d\omega}. \quad (58)$$

From the lossless boundary condition $F_0(i\omega_n^{(0)}) = -\omega_n^{(0)}B(\omega_n^{(0)}) + 1/L_J = 0$, we obtain $B_n \equiv B(\omega_n^{(0)}) = 1/(\omega_n^{(0)}L_J)$. Substituting into the derivative:

$$F_0'(i\omega_n^{(0)}) = \frac{i}{\omega_n^{(0)}L_J} - \omega_n^{(0)}B_n', \quad (59)$$

where $B_n' = dB/d\omega|_{\omega_n^{(0)}}$ is the slope of the susceptance at the mode frequency.

Substituting into Eq. (57) with $s_n^{(0)} = i\omega_n^{(0)}$:

$$\delta s = -\frac{\omega_n^{(0)}G_n}{\frac{1}{\omega_n^{(0)}L_J} + i\omega_n^{(0)}B_n'}, \quad (60)$$

where $G_n = G(\omega_n^{(0)})$ is the conductance at the mode frequency. To extract the real and imaginary parts, write the denominator as $D = D_R + iD_I$ with $D_R = 1/(\omega_n^{(0)}L_J)$ and $D_I = \omega_n^{(0)}B_n'$. Then

$$\delta s = -\frac{\omega_n^{(0)}G_n(D_R - iD_I)}{D_R^2 + D_I^2}. \quad (61)$$

The real part of δs gives the amplitude decay rate:

$$\text{Re}[\delta s] = -\frac{\omega_n^{(0)}G_n D_R}{D_R^2 + D_I^2} = -\frac{\kappa_n}{2}. \quad (62)$$

In the typical case where the susceptance varies rapidly near the mode frequency (corresponding to a high- Q resonance), we have $|D_I| \gg |D_R|$, and the decay rate simplifies to

$$\kappa_n = \frac{2G_n}{(\omega_n^{(0)} L_J)^2 (B'_n)^2 / (\omega_n^{(0)} L_J)}. \quad (63)$$

To express this more elegantly, we define the effective modal capacitance, which characterizes the mode's "inertia" as seen from the junction port:

$$C_n^{\text{eff}} \equiv \frac{1}{2\omega_n^{(0)}} \left. \frac{d(\omega B)}{d\omega} \right|_{\omega_n^{(0)}} = \frac{1}{2\omega_n^{(0)}} \left(B_n + \omega_n^{(0)} B'_n \right). \quad (64)$$

For modes where the susceptance slope dominates (typical of resonator modes with high quality factor), $\omega_n^{(0)} B'_n \gg B_n$, and $C_n^{\text{eff}} \approx B'_n/2$. Substituting this approximation into the decay rate formula yields the remarkably simple result

$$\kappa_n = \frac{G_n}{C_n^{\text{eff}}}. \quad (65)$$

This equation has a transparent circuit interpretation: the mode decay rate equals the conductance at the mode frequency divided by the effective capacitance, precisely the inverse RC time constant $\tau = RC$ with $\kappa = 1/\tau = G/C$. The effective capacitance C_n^{eff} measures how much charge must flow to change the junction voltage in mode n . For a simple LC resonator directly coupled to the junction, C_n^{eff} equals the physical capacitance. For more complex multimode environments, it incorporates the mode's participation in the network structure through the susceptance derivative.

The formula (65) also reveals the conditions for achieving long qubit lifetime: minimize the conductance $G(\omega_q)$ at the qubit frequency by engineering the environment to have low dissipation there, and maximize the effective capacitance by using modes with steep susceptance variation. Both conditions are naturally satisfied by Purcell filters, which create a band-stop response (low G) at the qubit frequency while maintaining high G at the readout frequency for fast measurement.

The imaginary part of δs gives the frequency shift due to dissipation:

$$\delta\omega_n = \text{Im}[\delta s] = \frac{G_n D_I}{D_R^2 + D_I^2} = \frac{G_n B'_n}{D_R^2 + D_I^2} \cdot \omega_n^{(0)}. \quad (66)$$

In the high- Q limit where $|D_I| \gg |D_R|$, this becomes $\delta\omega_n \approx G_n / (\omega_n^{(0)} B'_n)$. Comparing with the decay rate in the same limit, we find $\delta\omega_n / \kappa_n \sim B'_n / B_n \sim Q_n$, showing that the frequency shift is suppressed relative to the linewidth by the quality factor. For high- Q modes, the oscillation frequency remains well-defined even in the presence of dissipation, with the shift representing a small reactive loading effect from the dissipative environment.

V. CANONICAL QUANTIZATION

With the electromagnetic environment synthesized as a lumped circuit, we now construct the Lagrangian and Hamiltonian and carry out canonical quantization. The result is an exact quantum Hamiltonian retaining the full cosine nonlinearity of the Josephson potential.

A. The Circuit Lagrangian

Consider a synthesized circuit with M independent node fluxes Φ_1, \dots, Φ_M after eliminating any constraints from ideal transformers through symplectic reduction. The synthesized circuit is purely linear, arising from Foster or Brune synthesis of the positive-real admittance $Y_{\text{in}}(s)$. The Josephson junction contributes only the nonlinear cosine potential (69); its linear approximation (the Josephson inductance L_J) appeared in the boundary condition equation but is not part of the synthesized network. The capacitance matrix $C \in \mathbb{R}^{M \times M}$ and inverse inductance matrix $L^{-1} \in \mathbb{R}^{M \times M}$ are both real symmetric and positive-definite, reflecting the physical requirements of positive stored energy in capacitors and inductors.

The kinetic energy stored in the electric fields of all capacitors is

$$T = \frac{1}{2} \dot{\Phi}^T C \dot{\Phi} = \frac{1}{2} \sum_{i,j=1}^M C_{ij} \dot{\Phi}_i \dot{\Phi}_j, \quad (67)$$

where $\dot{\Phi} = (\dot{\Phi}_1, \dots, \dot{\Phi}_M)^T$ is the vector of node voltages. This quadratic form in the velocities plays the role of kinetic energy in the mechanical analogy, with the capacitance matrix acting as a generalized mass tensor.

The potential energy stored in the magnetic fields of all linear inductors is

$$U_{\text{lin}} = \frac{1}{2} \Phi^T L^{-1} \Phi = \frac{1}{2} \sum_{i,j=1}^M (L^{-1})_{ij} \Phi_i \Phi_j. \quad (68)$$

This quadratic form in the coordinates plays the role of potential energy, with the inverse inductance matrix acting as a generalized spring constant tensor.

The Josephson junction at node J contributes the nonlinear potential

$$U_J = -E_J \cos\left(\frac{\Phi_J}{\varphi_0}\right), \quad (69)$$

where Φ_J is the J -th component of the flux vector, corresponding to the junction node. This cosine potential has minima at $\Phi_J = 2\pi n \varphi_0$ for integer n , with curvature $E_J / \varphi_0^2 = 1/L_J$ at each minimum determining the Josephson inductance.

The total Lagrangian is the difference of kinetic and potential energies:

$$\mathcal{L} = T - U_{\text{lin}} - U_J = \frac{1}{2} \dot{\Phi}^T C \dot{\Phi} - \frac{1}{2} \Phi^T L^{-1} \Phi + E_J \cos\left(\frac{\Phi_J}{\varphi_0}\right). \quad (70)$$

This Lagrangian is exact in the sense that no approximation has been made to the Josephson nonlinearity. The full cosine potential is retained, which is essential for correctly describing the anharmonicity of the transmon spectrum, for treating regimes of ultrastrong coupling where phase fluctuations are not perturbatively small, and for capturing tunneling processes between adjacent potential wells at large drive amplitudes.

The Euler-Lagrange equations derived from this Lagrangian are

$$C\ddot{\Phi} + L^{-1}\Phi = -\frac{\partial U_J}{\partial \Phi} = \frac{E_J}{\varphi_0} \sin\left(\frac{\Phi_J}{\varphi_0}\right) e_J, \quad (71)$$

where e_J is the unit vector selecting the junction node. The right-hand side is nonzero only for the junction component, coupling the otherwise linear dynamics of the environmental modes to the nonlinear junction response.

B. Conjugate Momenta and the Hamiltonian

The conjugate momentum to the node flux Φ_i is defined by the partial derivative of the Lagrangian with respect to the velocity:

$$Q_i = \frac{\partial \mathcal{L}}{\partial \dot{\Phi}_i} = \sum_{j=1}^M C_{ij} \dot{\Phi}_j, \quad (72)$$

or in matrix form $Q = C\dot{\Phi}$. The physical interpretation is that Q_i represents the total charge at node i , which is the sum of charges on all capacitors connected to that node. This follows from the constitutive relation for capacitors: the current into a capacitor is $I = C\dot{V} = C\dot{\Phi}$, and integrating gives the charge $Q = C\dot{\Phi}$.

Since C is positive-definite and hence invertible, the velocity can be expressed in terms of the momentum: $\dot{\Phi} = C^{-1}Q$. The Hamiltonian is obtained via the Legendre transformation

$$H = Q^T C^{-1} Q - \frac{1}{2} Q^T C^{-1} Q + \frac{1}{2} \Phi^T L^{-1} \Phi - E_J \cos\left(\frac{\Phi_J}{\varphi_0}\right), \quad (73)$$

which simplifies to

$$H = \frac{1}{2} Q^T C^{-1} Q + \frac{1}{2} \Phi^T L^{-1} \Phi - E_J \cos\left(\frac{\Phi_J}{\varphi_0}\right). \quad (74)$$

We emphasize an important point regarding our conventions: under Assumption II.1, the junction capacitance C_J is already incorporated in the capacitance matrix C . No separate charging energy term $Q_J^2/(2C_J)$ should be added; doing so would double-count the junction capacitance and produce incorrect eigenfrequencies.

C. Normal Mode Decomposition

The linear part of the Hamiltonian describes coupled harmonic oscillators. To quantize the system, we must

first diagonalize this quadratic form by transforming to normal mode coordinates. This transformation decouples the linear dynamics, with all mode-mode coupling arising exclusively from the Josephson nonlinearity.

The linear Hamiltonian

$$H_{\text{lin}} = \frac{1}{2} Q^T C^{-1} Q + \frac{1}{2} \Phi^T L^{-1} \Phi \quad (75)$$

is a sum of two quadratic forms that are generally not simultaneously diagonal. The coupling arises because both C^{-1} and L^{-1} have off-diagonal elements when the circuit contains capacitive or inductive connections between different nodes.

To decouple these oscillators, we seek a coordinate transformation that simultaneously diagonalizes both quadratic forms. This is achieved by solving the generalized eigenvalue problem

$$L^{-1} \phi_n = \omega_n^2 C \phi_n, \quad (76)$$

where ω_n^2 are the eigenvalues (squared normal mode frequencies) and ϕ_n are the corresponding eigenvectors (mode shapes). The structure of this problem, with symmetric positive-definite matrices on both sides, guarantees favorable mathematical properties.

Proposition V.1 (Properties of the Generalized Eigenvalue Problem). *Let C and L^{-1} be real symmetric positive-definite $M \times M$ matrices. Then all eigenvalues ω_n^2 are real and strictly positive, the eigenvectors ϕ_n can be chosen to be real, and they satisfy the C-orthonormality condition $\phi_m^T C \phi_n = \delta_{mn}$ as well as the L^{-1} -diagonalization $\phi_m^T L^{-1} \phi_n = \omega_n^2 \delta_{mn}$.*

Proof. Since C is real symmetric positive-definite, it admits a Cholesky decomposition $C = R^T R$ where R is an invertible upper triangular matrix with positive diagonal entries. Define the transformed matrix $A \equiv R^{-T} L^{-1} R^{-1}$. This matrix is real symmetric because $A^T = (R^{-T} L^{-1} R^{-1})^T = R^{-T} (L^{-1})^T R^{-1} = R^{-T} L^{-1} R^{-1} = A$, using the symmetry of L^{-1} .

The generalized eigenvalue problem (76) transforms to the standard symmetric eigenvalue problem $A y_n = \omega_n^2 y_n$ under the substitution $y_n = R \phi_n$. Since A is real symmetric, its eigenvalues ω_n^2 are real and its eigenvectors y_n can be chosen real and orthonormal: $y_m^T y_n = \delta_{mn}$.

To show $\omega_n^2 > 0$, observe that A is positive-definite because L^{-1} is positive-definite: for any nonzero x , we have $x^T A x = x^T R^{-T} L^{-1} R^{-1} x = (R^{-1} x)^T L^{-1} (R^{-1} x) > 0$. Thus all eigenvalues of A are positive.

The original eigenvectors are $\phi_n = R^{-1} y_n$, which are real since both R^{-1} and y_n are real. The C-orthonormality follows from

$$\phi_m^T C \phi_n = y_m^T R^{-T} R^T R R^{-1} y_n = y_m^T y_n = \delta_{mn}. \quad (77)$$

The L^{-1} -diagonalization follows by multiplying the eigenvalue equation on the left by ϕ_m^T :

$$\phi_m^T L^{-1} \phi_n = \omega_n^2 \phi_m^T C \phi_n = \omega_n^2 \delta_{mn}. \quad (78)$$

□

Define the modal matrix $\Psi = (\phi_1 | \phi_2 | \dots | \phi_M) \in \mathbb{R}^{M \times M}$ whose columns are the C-orthonormal eigenvectors. The orthonormality conditions can be written compactly as $\Psi^T C \Psi = \mathbf{I}$ and $\Psi^T \mathbf{L}^{-1} \Psi = \Omega^2$ where $\Omega^2 = \text{diag}(\omega_1^2, \omega_2^2, \dots, \omega_M^2)$ is the diagonal matrix of squared frequencies.

The coordinate transformation from node fluxes to normal mode coordinates is defined by

$$\Phi(t) = \sum_{n=1}^M \xi_n(t) \phi_n = \Psi \xi(t), \quad (79)$$

where $\xi = (\xi_1, \dots, \xi_M)^T$ is the vector of normal mode coordinates. The inverse transformation is $\xi = \Psi^T C \Phi$, obtained by multiplying both sides of Eq. (79) by $\Psi^T C$ and using the C-orthonormality.

Under this transformation, the kinetic energy becomes

$$T = \frac{1}{2} \dot{\Phi}^T C \dot{\Phi} = \frac{1}{2} \dot{\xi}^T \Psi^T C \Psi \dot{\xi} = \frac{1}{2} \sum_{n=1}^M \dot{\xi}_n^2, \quad (80)$$

and the linear potential energy becomes

$$U_{\text{lin}} = \frac{1}{2} \Phi^T \mathbf{L}^{-1} \Phi = \frac{1}{2} \xi^T \Psi^T \mathbf{L}^{-1} \Psi \xi = \frac{1}{2} \sum_{n=1}^M \omega_n^2 \xi_n^2. \quad (81)$$

Both quadratic forms are now diagonal: each mode n behaves as an independent harmonic oscillator with unit effective mass (a consequence of the C-orthonormal convention) and frequency ω_n .

The junction flux Φ_J , which is the J -th component of the node flux vector, is expressed in terms of normal modes as

$$\Phi_J = (\Phi)_J = \sum_{n=1}^M \xi_n (\phi_n)_J \equiv \sum_{n=1}^M \xi_n \phi_n^J, \quad (82)$$

where the junction participation of mode n is defined as $\phi_n^J \equiv (\phi_n)_J$, the J -th component of the n -th eigenvector. This quantity determines how strongly mode n couples to the Josephson nonlinearity. A mode with $\phi_n^J = 0$ does not participate in the junction dynamics at all, while a mode with large $|\phi_n^J|$ couples strongly.

The conjugate momenta in the mode basis are simply $p_n = \partial \mathcal{L} / \partial \dot{\xi}_n = \dot{\xi}_n$, with the unit coefficient following from the C-orthonormal convention. The commutation relations $[\hat{\xi}_m, \hat{p}_n] = i\hbar \delta_{mn}$ are the standard canonical form, and the preservation of $[\hat{\Phi}_J, \hat{Q}_J] = i\hbar$ under the mode expansion can be verified using the completeness relation $\sum_n \phi_n \phi_n^T C = \mathbf{I}$.

D. The Exact Quantum Hamiltonian

Quantization proceeds by promoting the classical variables to operators satisfying canonical commutation

relations. In the mode basis, we introduce creation and annihilation operators through the standard relations

$$\hat{\xi}_n = \sqrt{\frac{\hbar}{2\omega_n}} (\hat{a}_n + \hat{a}_n^\dagger), \quad \hat{p}_n = i\sqrt{\frac{\hbar\omega_n}{2}} (\hat{a}_n^\dagger - \hat{a}_n), \quad (83)$$

with $[\hat{a}_m, \hat{a}_n^\dagger] = \delta_{mn}$ and $[\hat{a}_m, \hat{a}_n] = 0$. The linear Hamiltonian becomes $H_{\text{lin}} = \sum_n \hbar\omega_n (\hat{a}_n^\dagger \hat{a}_n + 1/2)$.

The junction flux operator is

$$\hat{\Phi}_J = \sum_{n=1}^M \phi_n^J \sqrt{\frac{\hbar}{2\omega_n}} (\hat{a}_n + \hat{a}_n^\dagger) = \sum_{n=1}^M \Phi_n^{J, \text{zpf}} (\hat{a}_n + \hat{a}_n^\dagger), \quad (84)$$

where $\Phi_n^{J, \text{zpf}} = \phi_n^J \sqrt{\hbar/(2\omega_n)}$ is the zero-point flux at the junction from mode n . The dimensionless coupling is $\lambda_n = \Phi_n^{J, \text{zpf}} / \varphi_0 = (\phi_n^J / \varphi_0) \sqrt{\hbar/(2\omega_n)}$.

The complete quantum Hamiltonian, dropping the constant zero-point energy $\sum_n \hbar\omega_n/2$, is

$$\hat{H} = \sum_{n=1}^M \hbar\omega_n \hat{a}_n^\dagger \hat{a}_n - E_J \cos\left(\frac{\hat{\Phi}_J}{\varphi_0}\right). \quad (85)$$

This is the central result of the quantization procedure.

Several features of this Hamiltonian deserve emphasis. First, the Hamiltonian retains the full cosine nonlinearity with no linearization, rotating-wave approximation, or truncation to two levels applied. The cosine $\cos(\hat{\Phi}_J/\varphi_0) = \cos(\sum_n \lambda_n (\hat{a}_n + \hat{a}_n^\dagger))$ contains all powers of the mode operators, including terms like $(\hat{a}_n + \hat{a}_n^\dagger)^4$ that generate Kerr nonlinearities, as well as counter-rotating products like $\hat{a}_m \hat{a}_n$ and $\hat{a}_m^\dagger \hat{a}_n^\dagger$ that are dropped in the rotating-wave approximation.

Second, the modes are decoupled in the linear part $\sum_n \hbar\omega_n \hat{a}_n^\dagger \hat{a}_n$, with all coupling between modes arising exclusively from the cosine nonlinearity through the junction participation ratios ϕ_n^J . This structure shows explicitly which physical process generates which coupling: the linear Hamiltonian describes independent oscillators, and the junction potential introduces all nonlinear corrections.

Third, no approximations have been made at the Hamiltonian level. The dispersive limit, strong coupling, ultrastrong coupling, and deep strong coupling regimes are all described by the same Hamiltonian (85); they differ only in which terms of the cosine expansion are numerically significant. The standard circuit QED parameters emerge as controlled limits of this exact theory, as developed in Section IX.

VI. ULTRAVIOLET CONVERGENCE

A fundamental concern in the quantization of circuits coupled to multimode environments is the convergence of sums over modes. Naive estimates suggest potential divergence: if the coupling to mode n scales as $g_n \propto \sqrt{\omega_n}$ from the vacuum fluctuation amplitude combined with capacitive coupling, then sums like

$\sum_n g_n^2/\omega_n$ might diverge logarithmically. This would render quantities like the Lamb shift infinite, requiring renormalization procedures borrowed from quantum field theory. In circuit QED, closely related ultraviolet concerns and their resolution by consistently modeling the linear environment rather than imposing an external cutoff have been addressed in a number of works, including early convergent models of capacitive coupling to infinite-dimensional circuits and subsequent impedance- and admittance-based quantization frameworks [3–5, 54].

In this section, we make this statement precise and prove a convergence theorem within the boundary-condition/admittance framework. Under the assumption that Y_{in} includes finite shunt capacitance at the junction node, the junction participation decays as ω_n^{-1} at high frequencies, ensuring absolute convergence of all physically relevant sums. The proof proceeds through careful analysis of the generalized eigenvalue problem for the synthesized circuit, exploiting the specific structure imposed by Foster synthesis and the boundary condition at the junction node.

A. Statement of Assumptions

The ultraviolet convergence theorem requires three assumptions, which we state explicitly to delineate the scope of the result.

Assumption VI.1 (Finite Shunt Capacitance). *The admittance $Y_{\text{in}}(s)$ includes a finite positive shunt capacitance $C_\Sigma > 0$ at the junction node, so that*

$$Y_{\text{in}}(i\omega) = i\omega C_\Sigma + Y_{\text{rem}}(i\omega), \quad (86)$$

where the remainder satisfies $|Y_{\text{rem}}(i\omega)| = O(1)$ as $\omega \rightarrow \infty$.

This assumption is automatically satisfied when the junction capacitance C_J is included in Y_{in} per Assumption II.1, since then $C_\Sigma \geq C_J > 0$. Physically, it states that the junction is not connected to a purely inductive environment, which would correspond to the unphysical limit of infinite impedance at high frequencies.

Assumption VI.2 (Finite Josephson Inductance). *The Josephson energy E_J is finite and positive, so the Josephson inductance $L_J = \varphi_0^2/E_J$ is finite and positive.*

This excludes the trivial case of no junction ($E_J = 0$, $L_J = \infty$) and the singular limit of infinite critical current ($E_J \rightarrow \infty$, $L_J \rightarrow 0$), both of which require separate treatment.

Assumption VI.3 (Positive-Real Admittance). *The admittance $Y_{\text{in}}(s)$ is positive-real, representing a physically realizable passive network.*

This assumption is guaranteed by the Schur complement construction from a passive multiport network

(Proposition III.1) and ensures that the synthesized circuit has positive-definite capacitance and inverse inductance matrices.

B. Structure of the Foster-Synthesized Circuit

Before proving the main theorem, we establish the specific structure of circuits arising from Foster synthesis, which is essential for the asymptotic analysis.

Consider a Foster-synthesized circuit with N resonant branches at frequencies $\omega_1 < \omega_2 < \dots < \omega_N$, plus a shunt capacitance C_Σ at the junction node as shown in Fig. 5. The circuit has $N + 1$ nodes: the junction node (labeled J) and one internal node for each LC branch (labeled $k = 1, \dots, N$). The node flux vector is $\Phi = (\Phi_J, \Phi_1, \dots, \Phi_N)^T$.

The capacitance matrix has the block structure

$$C = \begin{pmatrix} C_\Sigma & -C_1 & -C_2 & \dots & -C_N \\ -C_1 & C_1 & 0 & \dots & 0 \\ -C_2 & 0 & C_2 & \dots & 0 \\ \vdots & \vdots & \vdots & \ddots & \vdots \\ -C_N & 0 & 0 & \dots & C_N \end{pmatrix}, \quad (87)$$

where C_k is the capacitance of the k -th series LC branch. The off-diagonal elements $-C_k$ arise because each branch capacitor connects the junction node to the internal node of that branch. The (J, J) element $C_\Sigma = C_J + \sum_k C_k$ is the total capacitance connected to the junction node, confirming consistency with Assumption VI.1.

The inverse inductance matrix is diagonal:

$$L^{-1} = \text{diag}(L_J^{-1}, L_1^{-1}, L_2^{-1}, \dots, L_N^{-1}), \quad (88)$$

where L_J is the Josephson inductance and L_k is the inductance of the k -th branch, with the branch resonance condition $\omega_k^2 = 1/(L_k C_k)$. The diagonal structure of L^{-1} reflects that in Foster synthesis, each branch connects independently to ground through its inductor, with inductive coupling only through the shared junction node via the Josephson element.

C. Analysis of the Generalized Eigenvalue Problem

The dressed mode frequencies and shapes are determined by the generalized eigenvalue problem

$$L^{-1} \phi_n = \omega_n^2 C \phi_n, \quad (89)$$

with the C-orthonormality condition $\phi_n^T C \phi_n = 1$. Writing $\phi_n = (\phi_n^J, \phi_n^1, \dots, \phi_n^N)^T$, the eigenvalue equation decomposes into $N + 1$ scalar equations.

The equation at the junction node (J -th row) is

$$\frac{\phi_n^J}{L_J} = \omega_n^2 \left[C_\Sigma \phi_n^J - \sum_{k=1}^N C_k \phi_n^k \right]. \quad (90)$$

The equation at internal node k is

$$\frac{\phi_n^k}{L_k} = \omega_n^2 [-C_k \phi_n^J + C_k \phi_n^k] = \omega_n^2 C_k (\phi_n^k - \phi_n^J). \quad (91)$$

Rearranging the internal equation using $\omega_k^2 = 1/(L_k C_k)$:

$$\phi_n^k (\omega_k^2 - \omega_n^2) = -\omega_n^2 \phi_n^J, \quad (92)$$

which gives the internal node amplitude in terms of the junction amplitude:

$$\phi_n^k = \frac{\omega_n^2}{\omega_n^2 - \omega_k^2} \phi_n^J. \quad (93)$$

This is a key relation: the internal node amplitude ϕ_n^k is completely determined by the junction amplitude ϕ_n^J through a frequency-dependent factor. When $\omega_n \approx \omega_k$, the factor diverges, indicating that mode n is resonant with branch k and the mode is dominated by that branch. When $\omega_n \gg \omega_k$, the factor approaches unity: $\phi_n^k \rightarrow \phi_n^J$, meaning all internal nodes oscillate in phase with the junction at high frequencies.

D. Derivation of the Boundary Condition from the Eigenvalue Problem

Substituting the solution (93) into the junction equation (90):

$$\frac{\phi_n^J}{L_J} = \omega_n^2 \left[C_\Sigma \phi_n^J - \sum_{k=1}^N C_k \cdot \frac{\omega_n^2}{\omega_n^2 - \omega_k^2} \phi_n^J \right]. \quad (94)$$

For $\phi_n^J \neq 0$, dividing through gives

$$\frac{1}{L_J} = \omega_n^2 C_\Sigma - \sum_{k=1}^N \frac{\omega_n^4 C_k}{\omega_n^2 - \omega_k^2}. \quad (95)$$

To connect this to the admittance, recall the Foster form (44):

$$Y_{\text{in}}(s) = sC_\Sigma + \sum_{k=1}^N \frac{sC_k \omega_k^2}{s^2 + \omega_k^2}. \quad (96)$$

Evaluating at $s = i\omega_n$ and computing $sY_{\text{in}}(s)$:

$$i\omega_n Y_{\text{in}}(i\omega_n) = -\omega_n^2 C_\Sigma + \sum_{k=1}^N \frac{\omega_n^2 C_k \omega_k^2}{\omega_n^2 - \omega_k^2}. \quad (97)$$

The boundary condition $i\omega_n Y_{\text{in}}(i\omega_n) + 1/L_J = 0$ therefore reads

$$-\omega_n^2 C_\Sigma + \sum_{k=1}^N \frac{\omega_n^2 C_k \omega_k^2}{\omega_n^2 - \omega_k^2} + \frac{1}{L_J} = 0. \quad (98)$$

To verify consistency between Eqs. (95) and (98), we use the identity

$$\frac{\omega_n^4 C_k}{\omega_n^2 - \omega_k^2} = \omega_n^2 C_k + \frac{\omega_n^2 C_k \omega_k^2}{\omega_n^2 - \omega_k^2}, \quad (99)$$

which follows from adding and subtracting $\omega_n^2 C_k \omega_k^2$ in the numerator. Substituting into Eq. (95) and using $C_\Sigma = C_J + \sum_k C_k$:

$$\frac{1}{L_J} = \omega_n^2 C_J + \sum_{k=1}^N \frac{\omega_n^2 C_k \omega_k^2}{\omega_n^2 - \omega_k^2}, \quad (100)$$

which matches Eq. (98) with the junction capacitance C_J properly isolated. This confirms that the eigenvalue problem (89) is equivalent to the boundary condition equation, validating the use of either approach for determining mode frequencies.

E. The Normalization Constraint and Junction Participation

The C-orthonormality condition $\phi_n^T C \phi_n = 1$ provides the crucial constraint that determines the magnitude of ϕ_n^J . Expanding using the capacitance matrix structure (87):

$$1 = C_\Sigma (\phi_n^J)^2 - 2 \sum_{k=1}^N C_k \phi_n^J \phi_n^k + \sum_{k=1}^N C_k (\phi_n^k)^2. \quad (101)$$

Substituting the relation $\phi_n^k = \omega_n^2 \phi_n^J / (\omega_n^2 - \omega_k^2)$ from Eq. (93) and performing the algebra:

$$(\phi_n^k)^2 - 2\phi_n^J \phi_n^k = (\phi_n^J)^2 \cdot \frac{\omega_n^2 (2\omega_k^2 - \omega_n^2)}{(\omega_n^2 - \omega_k^2)^2}. \quad (102)$$

Substituting into the normalization condition and factoring out $(\phi_n^J)^2$:

$$(\phi_n^J)^2 = \frac{1}{C_\Sigma + \sum_{k=1}^N \frac{C_k \omega_n^2 (2\omega_k^2 - \omega_n^2)}{(\omega_n^2 - \omega_k^2)^2}}. \quad (103)$$

This exact expression determines the junction participation for any mode frequency ω_n . The ultraviolet behavior is determined by the asymptotic limit of this expression as $\omega_n \rightarrow \infty$.

F. High-Frequency Asymptotic Analysis

For $\omega_n \gg \max_k \omega_k$, we expand each term in the sum. Using $(1-x)^{-2} = 1 + 2x + O(x^2)$ for small $x = \omega_k^2/\omega_n^2$:

$$\frac{\omega_n^2 (2\omega_k^2 - \omega_n^2)}{(\omega_n^2 - \omega_k^2)^2} = \frac{2\omega_k^2/\omega_n^2 - 1}{(1 - \omega_k^2/\omega_n^2)^2} = -1 + \frac{4\omega_k^2}{\omega_n^2} + O(\omega_n^{-4}). \quad (104)$$

Summing over all branches gives

$$\sum_{k=1}^N \frac{C_k \omega_n^2 (2\omega_k^2 - \omega_n^2)}{(\omega_n^2 - \omega_k^2)^2} = -\sum_{k=1}^N C_k + \frac{4}{\omega_n^2} \sum_{k=1}^N C_k \omega_k^2 + O(\omega_n^{-4}). \quad (105)$$

Substituting into the denominator of Eq. (103) and using $C_\Sigma = C_J + \sum_k C_k$ yields

$$C_\Sigma - \sum_{k=1}^N C_k + O(\omega_n^{-2}) = C_J + O(\omega_n^{-2}). \quad (106)$$

Formally, this implies

$$(\phi_n^J)^2 = \frac{1}{C_J} (1 + O(\omega_n^{-2})), \quad (107)$$

which is the asymptotic behavior of the normalization factor *at fixed* ω_n .

However, Eq. (107) does *not* describe the behavior of physical eigenmodes at arbitrarily large frequency. The dressed frequencies ω_n are not free parameters but are determined by the boundary condition $sY_{\text{in}}(s) + 1/L_J = 0$. For a finite Foster network with N branches, this equation admits exactly $N + 1$ solutions, with the highest-frequency mode occurring near the plasma frequency $\omega_p = 1/\sqrt{L_J C_\Sigma}$ rather than at infinity. In the infinite-dimensional limit relevant to distributed environments or rational Foster sequences with $N \rightarrow \infty$, additional modes appear at higher frequencies, but the boundary condition forces their junction participation to decrease in order to maintain current balance at the junction node. As a result, physical eigenmodes with $\omega_n \gg \omega_p$ cannot realize the formal $O(1)$ behavior of Eq. (107); instead, their junction participation is suppressed, leading to the $O(\omega_n^{-1})$ (or faster) decay established in Theorem VI.4.

G. Mode Distribution and Participation Decay

To understand the decay of junction participation, it is helpful to separate two facts. First, the normalization constraint distributes amplitude across the circuit. Second, the boundary condition imposes a frequency-dependent constraint at the junction port.

Modes arising primarily from environmental resonances (i.e., dressed modes with ω_n close to some branch frequency ω_k) are dominated by the corresponding branch degree of freedom. This is already visible from Eq. (93): when $\omega_n \approx \omega_k$, the prefactor $\omega_n^2/(\omega_n^2 - \omega_k^2)$ becomes large, meaning the branch coordinate can dominate the C-normalization, while the junction component can remain comparatively small.

The ultraviolet statement concerns the opposite regime: dressed modes whose frequencies lie far above the junction plasma frequency $\omega_p = 1/\sqrt{L_J C_\Sigma}$. In that regime, the shunt capacitance at the port dominates the junction impedance, so the junction node is effectively shorted. In boundary-condition language,

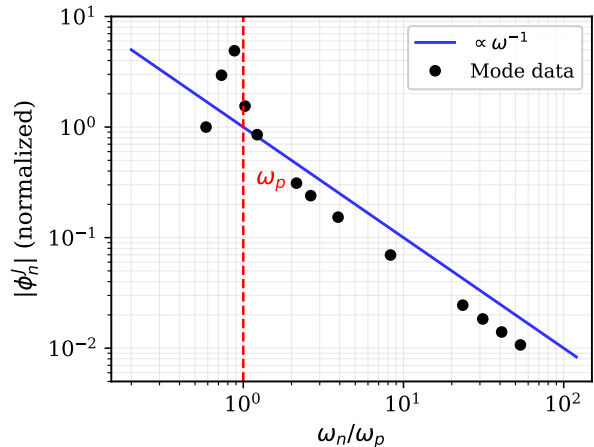


FIG. 7. Junction participation $|\phi_n^J|$ versus mode frequency demonstrating ultraviolet suppression. Black points show computed participation for dressed modes of a multimode Foster network with 50 branches; the blue line indicates the theoretical ω^{-1} scaling. Above the plasma frequency ω_p (red dashed line), the capacitive shunt at the junction node short-circuits high-frequency modes, causing their junction participation to decay. The scatter at low frequencies reflects mode-dependent coupling through the multimode environment, while the envelope follows the predicted asymptotic decay.

the port condition approaches a short-circuit constraint: high-frequency modes must have vanishing port voltage (hence vanishing junction flux) to satisfy current balance at the termination.

A clean way to see this is to examine the boundary condition $sY_{\text{in}}(s) + 1/L_J = 0$ for $s = i\omega$. Under Assumption VI.1,

$$Y_{\text{in}}(i\omega) = i\omega C_\Sigma + O(1), \quad \omega \rightarrow \infty, \quad (108)$$

so that

$$i\omega Y_{\text{in}}(i\omega) = -\omega^2 C_\Sigma + O(\omega). \quad (109)$$

If the junction coordinate had $O(1)$ participation at arbitrarily large ω_n , then the boundary condition would require a cancellation of the leading $-\omega_n^2 C_\Sigma$ term against $1/L_J$, which is impossible at fixed L_J . The only consistent resolution is that high-frequency dressed modes have suppressed junction participation, so that the port effectively sees a short and the junction degree of freedom decouples.

In practice, the suppression is at least $\phi_n^J = O(\omega_n^{-1})$ in the distributed/ infinite-dimensional limit, and typically faster in concrete geometries. This is the content of Theorem VI.4. The numerical data in Fig. 7 illustrates this behavior: above ω_p the junction participation falls with a clear envelope, so that increasing the number of retained modes yields convergent sums.

H. Main Theorem

Throughout this theorem, the asymptotic limit $\omega_n \rightarrow \infty$ is understood in an infinite-dimensional setting, such as a distributed electromagnetic environment, or along a sequence of rational Foster approximations with increasing order $N \rightarrow \infty$, for which the dressed spectrum contains modes of arbitrarily high frequency. At any fixed finite Foster order, the spectrum is bounded above by the plasma frequency and the ultraviolet limit does not arise.

Theorem VI.4 (Ultraviolet Suppression). *Under Assumptions VI.1, VI.2, and VI.3, the following hold for the dressed eigenmodes of the boundary condition equation (32):*

(i) **Junction participation decay:** *The junction component of the C-normalized mode shape satisfies*

$$\phi_n^J = O(\omega_n^{-1}) \quad \text{as } \omega_n \rightarrow \infty. \quad (110)$$

(ii) **Zero-point flux decay:** *The zero-point flux at the junction from mode n satisfies*

$$\Phi_n^{J,\text{zpf}} = O(\omega_n^{-3/2}) \quad \text{as } \omega_n \rightarrow \infty. \quad (111)$$

(iii) **Dimensionless coupling decay:** *The dimensionless coupling satisfies*

$$\lambda_n = O(\omega_n^{-3/2}) \quad \text{as } \omega_n \rightarrow \infty. \quad (112)$$

(iv) **Absolute convergence:** *All sums of the form $\sum_n \lambda_n^2 f(\omega_n)$ converge absolutely whenever $f(\omega) = O(\omega^k)$ with $k < 2$. In particular, the sum $\sum_n \lambda_n^2$ converges, the Lamb shift $\sum_n c_n \lambda_n^2 / |\omega_q - \omega_n|$ converges for bounded coefficients c_n , and the dispersive shift contributions $\sum_n \lambda_n^2 / (\omega_q - \omega_n)^2$ converge.*

Proof. Part (i): Under Assumption VI.1, the high-frequency asymptotic $sY_{\text{in}}(s) = s^2 C_\Sigma + O(s)$ implies that the boundary condition $sY_{\text{in}}(s) + 1/L_J = 0$ cannot be satisfied at arbitrarily large $|s|$ by modes with $O(1)$ junction participation. Equivalently, in the infinite-dimensional limit, any sequence of dressed modes with $\omega_n \rightarrow \infty$ must have suppressed junction component, yielding the envelope bound $\phi_n^J = O(\omega_n^{-1})$.

Part (ii): The zero-point flux is $\Phi_n^{J,\text{zpf}} = \phi_n^J \sqrt{\hbar} / (2\omega_n)$. With $\phi_n^J = O(\omega_n^{-1})$,

$$\Phi_n^{J,\text{zpf}} = O(\omega_n^{-3/2}). \quad (113)$$

Part (iii): The dimensionless coupling $\lambda_n = \Phi_n^{J,\text{zpf}} / \varphi_0$ therefore satisfies $\lambda_n = O(\omega_n^{-3/2})$.

Part (iv): With $\lambda_n^2 = O(\omega_n^{-3})$, the summand in $\sum_n \lambda_n^2 f(\omega_n)$ scales as $O(\omega_n^{k-3})$ when $f(\omega) = O(\omega^k)$. Absolute convergence follows when $k - 3 < -1$, i.e. $k < 2$, which covers all cases stated. \square

I. Physical Interpretation

The ultraviolet suppression has a direct physical interpretation: the junction capacitance short-circuits the junction node at high frequencies. At frequencies $\omega \gg \omega_p = 1/\sqrt{L_J C_\Sigma}$, the capacitive reactance $1/(\omega C_\Sigma)$ becomes much smaller than the Josephson inductive reactance ωL_J . Current preferentially flows through the capacitor rather than the junction, effectively bypassing the nonlinear element.

High-frequency modes therefore see a nearly short-circuited boundary condition at the junction, forcing their electric field (and hence flux) to vanish there. This is analogous to the electromagnetic boundary condition at a perfect conductor, where the tangential electric field vanishes. In the circuit context, the capacitive shunt provides this short-circuit behavior at high frequencies, with the transition occurring near the plasma frequency.

The mathematical structure revealed by the proof is that the junction participation ϕ_n^J is determined by two competing effects: the normalization constraint, which distributes mode amplitude across the circuit, and the boundary condition at the junction, which suppresses junction participation for modes whose frequency is incompatible with the junction's characteristic impedance $Z_J = \sqrt{L_J / C_\Sigma}$. For modes near the plasma frequency, both constraints can be satisfied with $O(1)$ junction participation. For modes far above the plasma frequency, the boundary condition forces suppression, leading to the $O(\omega_n^{-1})$ or faster decay.

The theorem guarantees that increasing the number of modes in a rational fit or numerical calculation yields convergent results. The truncation error from neglecting modes above frequency ω_{max} scales as

$$\epsilon \sim \sum_{n:\omega_n > \omega_{\text{max}}} \lambda_n^2 \sim \int_{\omega_{\text{max}}}^{\infty} \omega^{-3} d\omega \sim \omega_{\text{max}}^{-2}. \quad (114)$$

This rapid convergence ($\propto \omega_{\text{max}}^{-2}$) means that including modes up to a few times the plasma frequency suffices for accurate results, typically requiring only 10–20 modes for percent-level accuracy in physical observables.

VII. MULTI-MODE INTERFERENCE AND PURCELL SUPPRESSION

In realistic circuits, multiple electromagnetic modes couple to the junction, and interference between decay pathways can significantly modify or completely suppress the effective Purcell rate [55, 56]. This section derives the multi-mode interference formula directly from the boundary-condition admittance, demonstrating that the framework naturally captures coherent pathway interference without additional phenomenological assumptions. The central result is that the qubit decay rate is determined by the real part of the admittance evaluated at the qubit frequency, weighted by

the junction participation. When multiple modes contribute to this admittance, their contributions can interfere constructively or destructively depending on the relative phases and detunings, and this interference is encoded entirely in the structure of the admittance function $Y_{\text{in}}(s)$.

A. Purcell Decay from the Boundary Condition Perspective

The Purcell effect describes the modification of spontaneous emission rates when an emitter is coupled to a structured electromagnetic environment. For a qubit coupled to a resonator, the qubit can decay by emitting a photon into the resonator, which subsequently leaks to the external environment. The decay rate depends on the spectral density of the environment at the qubit frequency, and in the boundary condition framework, this spectral density is encoded in the admittance $Y_{\text{in}}(s)$ seen at the junction.

The real part $G(\omega) = \text{Re}[Y_{\text{in}}(i\omega)]$ represents dissipation, quantifying the rate at which energy injected at frequency ω is absorbed by the environment. The Purcell decay rate is therefore controlled by $G(\omega_q)$, the conductance at the qubit frequency. This connection can be derived rigorously from Fermi's golden rule, which gives the transition rate from an initial state $|i\rangle$ to a continuum of final states $|f\rangle$ as

$$\Gamma = \frac{2\pi}{\hbar} \sum_f |\langle f | \hat{H}_{\text{int}} | i \rangle|^2 \delta(E_f - E_i). \quad (115)$$

For the qubit-environment system, the interaction Hamiltonian in the linearized approximation takes the form $\hat{H}_{\text{int}} = (\hat{\Phi}_J/L_J) \cdot \hat{\Phi}_{\text{env}}$, where $\hat{\Phi}_J$ is the junction flux operator and $\hat{\Phi}_{\text{env}}$ represents the environmental degrees of freedom. The fluctuation-dissipation theorem relates the symmetrized noise spectral density of the environment to the real part of the admittance through

$$S_{\Phi\Phi}(\omega) = \hbar \coth\left(\frac{\hbar\omega}{2k_B T}\right) \text{Re}[Z_{\text{env}}(i\omega)], \quad (116)$$

where $Z_{\text{env}} = 1/Y_{\text{env}}$ is the environmental impedance excluding the junction.

At zero temperature, the decay rate from the excited qubit state $|e\rangle$ to the ground state $|g\rangle$ becomes

$$\Gamma = \frac{1}{\hbar^2} |\langle g | \hat{\Phi}_J | e \rangle|^2 \cdot \text{Re}[Y_{\text{env}}(i\omega_q)] \cdot \hbar\omega_q. \quad (117)$$

The matrix element $|\langle g | \hat{\Phi}_J | e \rangle|^2$ is determined by the qubit's zero-point flux fluctuation, which for a transmon in the harmonic approximation gives $|\langle g | \hat{\Phi}_J | e \rangle|^2 = (\Phi_q^{\text{zpf}})^2 = \hbar/(2\omega_q C_q^{\text{eff}})$, where C_q^{eff} is the effective capacitance of the qubit mode. Substituting this result yields

$$\Gamma = \frac{\omega_q}{2C_q^{\text{eff}}} \text{Re}[Y_{\text{env}}(i\omega_q)]. \quad (118)$$

This fundamental result connects the qubit decay rate directly to the real part of the environmental admittance at the qubit frequency. In the boundary condition framework, the total admittance seen by the junction is $Y_{\text{in}}(s)$, which includes the junction capacitance C_J . The environmental admittance entering Eq. (118) is therefore $Y_{\text{env}}(s) = Y_{\text{in}}(s) - sC_J$, where we subtract the junction capacitance contribution since it represents reactive energy storage rather than dissipation to the external environment. For a lossless junction capacitance, $\text{Re}[sC_J]|_{s=i\omega} = 0$, so $\text{Re}[Y_{\text{env}}(i\omega_q)] = \text{Re}[Y_{\text{in}}(i\omega_q)] = G(\omega_q)$, and the decay rate becomes

$$\Gamma = \frac{\omega_q G(\omega_q)}{2C_q^{\text{eff}}}. \quad (119)$$

This result demonstrates that the Purcell rate is determined by two quantities obtained directly from the boundary condition framework: the conductance $G(\omega_q) = \text{Re}[Y_{\text{in}}(i\omega_q)]$, which encodes the dissipative response of the environment, and the effective capacitance C_q^{eff} , which is related to the derivative of the susceptance at the qubit frequency as derived in Section IV D.

B. Single-Mode Purcell Formula from the Boundary Condition

Before treating the multi-mode case, we derive the standard single-mode Purcell formula from the boundary condition framework to establish the connection to conventional circuit QED results. Consider a single resonator mode at frequency ω_r with decay rate κ , capacitively coupled to the junction with coupling capacitance C_g . The resonator's admittance, including its loss, is modeled as a parallel RLC circuit with $Y_r(s) = 1/R_r + sC_r + 1/(sL_r)$, where $\omega_r = 1/\sqrt{L_r C_r}$ and the quality factor is $Q_r = \omega_r C_r R_r$.

Near resonance, the admittance can be written as $Y_r(i\omega) \approx (\kappa_r C_r/2) + 2iC_r(\omega - \omega_r)$ for $|\omega - \omega_r| \ll \omega_r$, where $\kappa_r = 1/(R_r C_r) = \omega_r/Q_r$ is the resonator linewidth. The total admittance seen by the junction, including the coupling network, is obtained from the Schur complement reduction developed in Section III. For simple capacitive coupling, this yields

$$Y_{\text{in}}(s) = sC_J + \frac{s^2 C_g^2}{sC_g + Y_r(s)}. \quad (120)$$

At the qubit frequency ω_q with $s = i\omega_q$, we have $Y_{\text{in}}(i\omega_q) = i\omega_q C_J + (-\omega_q^2 C_g^2)/[i\omega_q C_g + Y_r(i\omega_q)]$. To find the decay rate, we need $G(\omega_q) = \text{Re}[Y_{\text{in}}(i\omega_q)]$. The first term $i\omega_q C_J$ is purely imaginary and does not contribute. For the second term, we write $Y_r(i\omega_q) = G_r + iB_r$ where $G_r = \text{Re}[Y_r(i\omega_q)]$ and $B_r = \text{Im}[Y_r(i\omega_q)] \approx 2C_r(\omega_q - \omega_r)$.

In the dispersive regime where $|\omega_q - \omega_r| \gg \kappa_r$, the resonator conductance at the qubit frequency is $G_r \approx \kappa_r C_r \omega_r^2 / [4(\omega_q - \omega_r)^2]$. The second term in $Y_{\text{in}}(i\omega_q)$ becomes $(-\omega_q^2 C_g^2)/(G_r + i(\omega_q C_g + B_r))$, and extracting the

real part gives

$$\text{Re} \left[\frac{-\omega_q^2 C_g^2}{G_r + i(\omega_q C_g + B_r)} \right] = \frac{-\omega_q^2 C_g^2 \cdot G_r}{G_r^2 + (\omega_q C_g + B_r)^2}. \quad (121)$$

In the dispersive limit where $|B_r| \gg G_r$ and $|B_r| \gg \omega_q C_g$, this simplifies to $G(\omega_q) \approx \omega_q^2 C_g^2 G_r / B_r^2$. Substituting the expressions for G_r and B_r and using the coupling strength $g = \omega_q C_g / (2\sqrt{C_J C_r})$ derived in Section IX, we obtain

$$\Gamma_{\text{Purcell}} = \frac{g^2 \kappa_r}{\Delta^2 + (\kappa_r/2)^2}, \quad (122)$$

where $\Delta = \omega_q - \omega_r$ is the qubit-resonator detuning. This is the standard Purcell formula, now derived directly from the boundary condition framework. The physical interpretation is clear: the Purcell rate is determined by the conductance of the environment at the qubit frequency, which in turn depends on how much of the resonator's dissipation is "seen" by the junction through the coupling network.

C. Multi-Mode Admittance and the Matrix Resolvent

We now generalize to an electromagnetic environment containing M modes, deriving the multi-mode admittance and its implications for qubit decay. Consider a Foster-synthesized network with M resonant branches at frequencies $\omega_1, \omega_2, \dots, \omega_M$, where each branch has finite quality factor Q_k . The admittance takes the form

$$Y_{\text{in}}(s) = sC_\Sigma + \sum_{k=1}^M \frac{sC_k \omega_k^2}{s^2 + s\kappa_k + \omega_k^2}, \quad (123)$$

where $\kappa_k = \omega_k / Q_k$ is the linewidth of mode k and $C_\Sigma = C_J + \sum_k C_k$ is the total shunt capacitance.

Evaluating at $s = i\omega$ and separating real and imaginary parts, the conductance becomes

$$G(\omega) = \sum_{k=1}^M \frac{\omega^2 C_k \omega_k^2 \kappa_k}{(\omega_k^2 - \omega^2)^2 + \omega^2 \kappa_k^2}. \quad (124)$$

Near mode k where $\omega \approx \omega_k$, we can approximate $\omega_k^2 - \omega^2 \approx 2\omega_k(\omega_k - \omega)$, giving a sum of Lorentzian peaks centered at each mode frequency ω_k with width κ_k and height $C_k \omega_k^2 / \kappa_k$.

When inter-mode coupling is present, the analysis requires the matrix resolvent formulation. The dynamics of N environmental modes with inter-mode coupling are described by the mode matrix $M \in \mathbb{C}^{N \times N}$ with diagonal elements $M_{kk} = i\omega_k + \kappa_k/2$ combining the oscillation frequency with the amplitude decay rate, and off-diagonal elements $M_{kl} = iJ_{kl}e^{i\theta_{kl}}$ representing coherent inter-mode coupling with strength J_{kl} and phase θ_{kl} . The junction couples to each mode with a complex

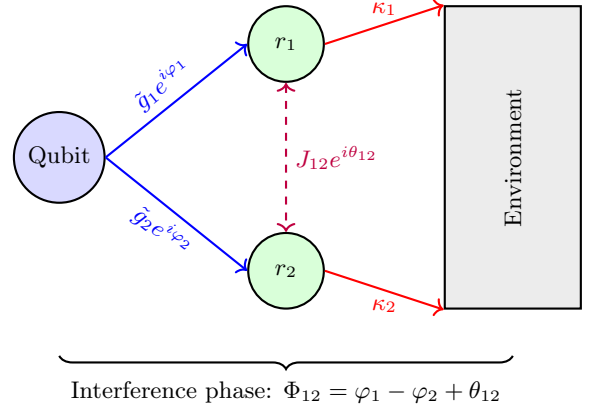


FIG. 8. Multi-mode Purcell interference geometry. The qubit couples to two environmental modes r_1 and r_2 with complex amplitudes $\tilde{g}_k e^{i\varphi_k}$ determined by the junction participation and mode phase at the junction location. Inter-mode coupling $J_{12}e^{i\theta_{12}}$ creates alternative decay pathways that can interfere with direct decay. Both modes decay to a common environment with rates κ_1 and κ_2 . The total decay rate depends on the interference phase $\Phi_{12} = \varphi_1 - \varphi_2 + \theta_{12}$, which combines the junction coupling phases with the inter-mode coupling phase.

amplitude forming the coupling vector $\mathbf{g} \in \mathbb{C}^M$ with components $g_k = \tilde{g}_k e^{i\varphi_k}$, where $\tilde{g}_k = \omega_k \phi_k^J / \sqrt{2}$ is the coupling magnitude proportional to the junction participation and φ_k is the phase of mode k at the junction.

The geometry of multi-mode interference is illustrated in Fig. 8, showing how the qubit couples to multiple environmental modes that subsequently decay through a common port. The interference between different decay pathways depends on the phases accumulated along each path, which combine into a total interference phase $\Phi_{kl} = \varphi_l - \varphi_k + \theta_{kl}$ for pathways involving modes k and l .

The admittance seen by the junction can be expressed in terms of the mode matrix and coupling vector as

$$Y_{\text{in}}(s) = sC_\Sigma + \frac{1}{L_J} \mathbf{g}^\dagger (s\mathbf{I} - M)^{-1} \mathbf{g}, \quad (125)$$

where \mathbf{I} is the $M \times M$ identity matrix and the factor $1/L_J$ converts flux to current. The first term represents the direct capacitive admittance at the junction, while the second term represents the admittance due to current flowing through the junction, exciting the environmental modes, propagating through the coupled mode system via the resolvent $(s\mathbf{I} - M)^{-1}$, and returning through the coupling vectors \mathbf{g} .

D. Perturbative Expansion and Interference Terms

When the inter-mode couplings J_{kl} are weak compared to the mode separations $|\omega_k - \omega_l|$, the resolvent can be expanded perturbatively to reveal the structure

of interference contributions. Writing the mode matrix as $M = D + J$ where $D = \text{diag}(i\omega_1 + \kappa_1/2, \dots, i\omega_M + \kappa_M/2)$ is diagonal and J contains the off-diagonal inter-mode couplings, we define $\tilde{D} \equiv i\omega_q I - D$ with diagonal elements $\tilde{D}_k = i\Delta_k - \kappa_k/2$ where $\Delta_k = \omega_q - \omega_k$ is the detuning from mode k .

The resolvent factorizes as $(i\omega_q I - M)^{-1} = (\tilde{D} - J)^{-1} = \tilde{D}^{-1}(I - \tilde{D}^{-1}J)^{-1}$, and for $\|\tilde{D}^{-1}J\| < 1$ we can expand in a Neumann series to obtain

$$(i\omega_q I - M)^{-1} = \tilde{D}^{-1} + \tilde{D}^{-1}J\tilde{D}^{-1} + \tilde{D}^{-1}J\tilde{D}^{-1}J\tilde{D}^{-1} + O(J^3). \quad (126)$$

The qubit self-energy, which determines the decay rate through $\Gamma = -2\text{Im}[\Sigma(\omega_q)]$, is given by $\Sigma(\omega_q) = (\omega_q/L_J)g^\dagger(i\omega_q I - M)^{-1}g$. The zeroth-order contribution from the first term in Eq. (126) gives

$$\Sigma^{(0)} = \frac{\omega_q}{L_J} \sum_{k=1}^M \frac{\tilde{g}_k^2}{i\Delta_k - \kappa_k/2}, \quad (127)$$

whose imaginary part yields the direct Purcell contribution

$$\Gamma^{(0)} = \sum_{k=1}^M \frac{\omega_q \tilde{g}_k^2 \kappa_k}{L_J [\Delta_k^2 + (\kappa_k/2)^2]} = \sum_{k=1}^M \frac{g_k^2 \kappa_k}{\Delta_k^2 + (\kappa_k/2)^2}. \quad (128)$$

This is the incoherent sum of individual Purcell rates from each mode, confirming that the zeroth-order term reproduces the standard multi-mode result without interference.

The first-order correction from the second term in Eq. (126) is

$$\Sigma^{(1)} = \frac{\omega_q}{L_J} \sum_{k \neq l} \frac{\tilde{g}_k \tilde{g}_l J_{kl} e^{i\Phi_{kl}}}{\tilde{D}_k \tilde{D}_l}, \quad (129)$$

where $\Phi_{kl} = \varphi_l - \varphi_k + \theta_{kl}$ is the total interference phase for the (k, l) pathway. To extract the decay rate contribution, we compute the product $1/(\tilde{D}_k \tilde{D}_l) = 1/[(i\Delta_k - \kappa_k/2)(i\Delta_l - \kappa_l/2)]$. Rationalizing this expression gives

$$\frac{1}{\tilde{D}_k \tilde{D}_l} = \frac{-\Delta_k \Delta_l + \kappa_k \kappa_l / 4 - i(\Delta_k \kappa_l + \Delta_l \kappa_k) / 2}{[\Delta_k^2 + (\kappa_k/2)^2][\Delta_l^2 + (\kappa_l/2)^2]}. \quad (130)$$

The interference contribution to the decay rate involves both the real and imaginary parts of this expression combined with $\cos \Phi_{kl}$ and $\sin \Phi_{kl}$ from the phase factor. After carrying out the algebra, the result is

$$\Gamma_{kl}^{\text{int}} = \frac{2\omega_q \tilde{g}_k \tilde{g}_l J_{kl}}{L_J} \cdot \frac{(\kappa_k \Delta_l + \kappa_l \Delta_k) \cos \Phi_{kl} + 2(\Delta_k \Delta_l - \kappa_k \kappa_l / 4) \sin \Phi_{kl}}{[\Delta_k^2 + (\kappa_k/2)^2][\Delta_l^2 + (\kappa_l/2)^2]}. \quad (131)$$

In the limit where the linewidths are small compared to detunings, this simplifies to

$$\Gamma_{kl}^{\text{int}} \approx \frac{2\omega_q \tilde{g}_k \tilde{g}_l J_{kl}}{L_J} \cdot \frac{(\kappa_k \Delta_l + \kappa_l \Delta_k) \cos \Phi_{kl}}{\Delta_k^2 \Delta_l^2}. \quad (132)$$

The complete decay rate combining direct and interference contributions is therefore

$$\Gamma_{\text{eff}} = \sum_{k=1}^M \Gamma_k^{\text{direct}} + \sum_{k < l} \Gamma_{kl}^{\text{int}}, \quad (133)$$

where the first sum contains positive direct Purcell contributions from each mode and the second sum contains interference terms that can be positive or negative depending on the interference phase Φ_{kl} , the signs of the detunings Δ_k and Δ_l , and the relative magnitudes of the linewidths κ_k and κ_l .

E. Conditions for Purcell Suppression

Complete suppression of Purcell decay requires the interference terms to exactly cancel the direct contributions, which demands $\Gamma_{kl}^{\text{int}} = -(\Gamma_k^{\text{direct}} + \Gamma_l^{\text{direct}})$ for the two-mode case. Since the direct contributions are positive, this requires destructive interference with $\Gamma_{kl}^{\text{int}} < 0$.

From Eq. (132), destructive interference occurs when $(\kappa_k \Delta_l + \kappa_l \Delta_k) \cos \Phi_{kl} < 0$. This condition can be satisfied in several ways. If the qubit frequency lies between the two mode frequencies so that Δ_k and Δ_l have opposite signs, then $(\kappa_k \Delta_l + \kappa_l \Delta_k)$ can be made negative with appropriate asymmetry in the linewidths, and $\cos \Phi_{kl} > 0$ gives destructive interference. Alternatively, if both detunings have the same sign, $\cos \Phi_{kl} < 0$ (achieved with Φ_{kl} near π) produces the required negative interference term.

Several necessary conditions must be satisfied for complete Purcell suppression. First, non-zero inter-mode coupling is essential: if $J_{kl} = 0$ then $\Gamma_{kl}^{\text{int}} = 0$ and no interference occurs. The inter-mode coupling creates alternative decay pathways that can interfere with direct decay. Second, asymmetric detunings are required: the interference term contains the factor $(\kappa_k \Delta_l + \kappa_l \Delta_k)$, which vanishes when $\Delta_k = -\Delta_l$ and $\kappa_k = \kappa_l$, eliminating the interference contribution. Third, appropriate phase alignment is necessary: the phase factor $\cos \Phi_{kl}$ must have the correct sign for destructive interference, requiring engineering of the relative phases of the mode fields at the junction and the inter-mode coupling phase. Fourth, magnitude matching is required: even with the correct sign, the interference term must be large enough to cancel the direct terms, demanding sufficient inter-mode coupling strength.

Purcell suppression occurs at discrete frequencies where the algebraic conditions are satisfied, corresponding to transmission zeros in the real part of the admittance $G(\omega)$. Setting $G(\omega) = 0$ and solving for ω gives the suppression frequencies. Since each term in the direct Purcell sum (124) is positive for a passive network without inter-mode coupling, the equation $G(\omega) = 0$ has no real solutions in that case. With inter-mode coupling, the modified admittance can develop zeros corresponding to frequencies where destructive interference completely suppresses dissipation.

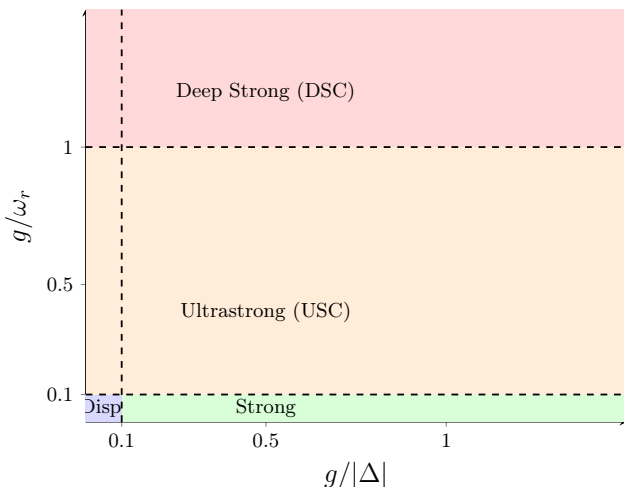


FIG. 9. Coupling regime phase diagram. The dispersive regime (blue) requires both $g/|\Delta| < 0.1$ and $g/\omega_r < 0.1$. Strong coupling (green) has $g/|\Delta| \gtrsim 0.1$ but $g/\omega_r < 0.1$, so the RWA remains valid. Ultrastrong coupling (USC, orange) has $0.1 \lesssim g/\omega_r < 1$, requiring counter-rotating terms. Deep strong coupling (DSC, red) has $g/\omega_r \gtrsim 1$.

VIII. COUPLING REGIMES FROM THE BOUNDARY CONDITION FRAMEWORK

The boundary condition framework provides a unified treatment that does not rely on rotating-wave or dispersive approximations at the Hamiltonian level. Different coupling regimes are distinguished by which terms in the cosine expansion are numerically significant, not by changes to the framework itself. Before deriving the standard circuit QED parameters as limits, it is essential to delineate the regimes where different approximations apply. The relevant dimensionless parameters are the normalized coupling g/ω_r , the ratio $g/|\Delta|$ characterizing perturbative validity, and for the transmon, the ratio E_J/E_C . Different combinations define qualitatively distinct physical regimes [12]. Figure 9 maps the coupling regime phase diagram, delineating where different approximations apply based on the dimensionless ratios $g/|\Delta|$ and g/ω_r .

A. The Dispersive Regime

The dispersive regime is characterized by the hierarchy $g \ll |\Delta|$, meaning the coupling is weak compared to the qubit-resonator detuning. The standard criterion is

$$\frac{g}{|\Delta|} < 0.1, \quad (134)$$

with typical experimental values in the range 0.01–0.05. Additionally, the rotating-wave approximation requires

$$\frac{g}{\omega_r} \ll 0.1, \quad (135)$$

with typical experimental values well below this threshold.

In this regime, qubit and resonator states remain well-defined product states $|g, n\rangle$, $|e, n\rangle$ with only perturbative mixing. The qubit-state-dependent frequency shift of the resonator enables dispersive readout. The validity conditions for the dispersive shift formula $\chi = g^2\alpha/[\Delta(\Delta + \alpha)]$ are:

1. Weak coupling relative to detuning: $g/|\Delta| \ll 1$
2. Rotating-wave approximation valid: $g \ll \omega_q, \omega_r$
3. No level crossings: the qubit frequency is not near any dressed cavity mode
4. The two-level approximation is valid provided that higher transmon levels are far detuned, satisfying $|\Delta_{ef}| \gg g\sqrt{2}$, where $\Delta_{ef} = \omega_{ef} - \omega_r$

Within the boundary condition framework, the dispersive regime corresponds to the parameter range where the cosine expansion to quartic order is accurate and the bilinear coupling can be projected onto the excitation-exchange sector.

B. The Strong Coupling Regime

The strong coupling regime is defined by

$$g > \kappa, \gamma, \quad (136)$$

where κ is the resonator decay rate and γ is the qubit decay rate. This ensures coherent qubit-resonator dynamics occurs faster than decoherence, enabling observation of vacuum Rabi oscillations.

A more stringent definition for the purpose of approximation validity is

$$\frac{g}{|\Delta|} \gtrsim 0.1, \quad (137)$$

at which point higher-order corrections to the dispersive formula become non-negligible.

In strong coupling, the eigenstates are no longer product states but dressed states with significant qubit-resonator entanglement. Near resonance $\Delta \rightarrow 0$, the dressed states approach the symmetric and antisymmetric superpositions

$$|\pm, n\rangle = \frac{1}{\sqrt{2}} (|g, n+1\rangle \pm |e, n\rangle), \quad (138)$$

split by the vacuum Rabi frequency $2g\sqrt{n+1}$.

The boundary condition equation captures this physics exactly. The poles of the admittance, which determine dressed mode frequencies, exhibit avoided crossings as the qubit frequency is tuned through resonance with the cavity. The minimum separation at the avoided crossing equals the vacuum Rabi splitting $2g$.

Remark VIII.1. *The breakdown of bare-mode descriptions in the strong-coupling regime is well known in classical microwave filter theory. For strongly interacting resonator posts, equivalent circuits based on individual post resonances fail, and one must instead work with the electromagnetic eigenmodes that satisfy the full boundary conditions [59]. The present quantum circuit analysis exhibits the same structure: when $g/|\Delta| \gtrsim 0.3$, coupling constants defined between bare qubit and resonator modes lose physical meaning, and one must work directly with the dressed polariton modes obtained from the boundary-condition framework.*

C. The Ultrastrong Coupling (USC) Regime

The ultrastrong coupling regime is defined by

$$0.1 \lesssim \frac{g}{\omega_r} < 1. \quad (139)$$

In this regime, the coupling strength becomes comparable to the bare mode frequencies, and the rotating-wave approximation breaks down completely. Counter-rotating terms $\hat{a}\hat{b}$ and $\hat{a}^\dagger\hat{b}^\dagger$ that create or destroy pairs of excitations can no longer be neglected.

The physical consequences of ultrastrong coupling are profound:

Ground state photons. The ground state is no longer the vacuum $|0, g\rangle$ but contains virtual photon-qubit pairs, with mean photon number scaling as

$$\langle \hat{n} \rangle_{\text{gs}} \sim \left(\frac{g}{\omega_r} \right)^2. \quad (140)$$

Bloch-Siegert shift. The leading correction from counter-rotating terms shifts the qubit frequency by

$$\delta\omega_q^{\text{BS}} = \frac{g^2}{\omega_q + \omega_r}. \quad (141)$$

For $g/\omega_r = 0.1$ and $\omega_q \approx \omega_r$, this shift is approximately 0.5% of the mode frequency, small but measurable.

Breakdown of excitation number conservation. The total excitation number $\hat{N} = \hat{a}^\dagger\hat{a} + \hat{b}^\dagger\hat{b}$ is no longer conserved because counter-rotating terms create and annihilate excitation pairs.

The boundary condition framework handles the USC regime without modification because the exact Hamiltonian (85) retains the full cosine nonlinearity, which contains all powers of the phase operator including counter-rotating contributions. No rotating-wave approximation is made at the Hamiltonian level; the RWA emerges only as a controlled limit when deriving the Jaynes-Cummings model in Section IX.

D. The Deep Strong Coupling (DSC) Regime

The deep strong coupling regime corresponds to

$$\frac{g}{\omega_r} \gtrsim 1. \quad (142)$$

This extreme regime has been achieved in certain platforms including flux qubits coupled to LC oscillators [57] and Landau polaritons in semiconductor systems [58].

In DSC, the physics is dominated by counter-rotating terms, and perturbative treatments fail entirely. The ground state contains order-unity photon populations, and the spectrum differs qualitatively from the Jaynes-Cummings ladder. The boundary condition framework remains formally applicable, though numerical diagonalization of the Hamiltonian with many Fock states may be required.

E. Summary of Coupling Regimes

Table I summarizes the coupling regimes and their characteristics.

TABLE I. Summary of coupling regimes in circuit QED.

Regime	$g/ \Delta $	g/ω_r	Key features
Dispersive	< 0.1	< 0.1	Dispersive approximation valid
Strong	$\gtrsim 0.1$	< 0.1	Dressed states, JC valid
USC	any	0.1–1	Counter-rotating terms significant
DSC	any	> 1	Photonic ground state

The boundary condition framework provides a unified starting point for all regimes. The exact Hamiltonian (85) with full cosine nonlinearity is valid throughout; the dispersive and Jaynes-Cummings formulas emerge as controlled approximations valid when the appropriate small parameters are satisfied. Outside these limits, the exact Hamiltonian must be used, but the framework itself requires no modification.

IX. STANDARD CIRCUIT QED RESULTS AS LIMITS

With the exact Hamiltonian (85) and the ultraviolet convergence established, we now connect to the familiar territory of circuit QED. The dispersive shift χ , the coupling strength g , and the anharmonicity α are the quantities that appear in experimental design, calibration, and data analysis. Deriving them from the exact theory serves two purposes: it validates the approximations underlying standard circuit QED formulas, and it clarifies precisely when those approximations fail.

The strategy is systematic expansion with explicit validity conditions. The cosine potential is expanded in powers of the phase; the rotating-wave approximation drops rapidly oscillating terms; the dispersive limit treats the qubit-resonator coupling perturbatively. At each step, we state the approximation and its domain of validity. The standard formulas emerge at the end, understood as controlled limits rather than starting assumptions.

A. Expansion of the Cosine Potential

The cosine potential is expanded as a Taylor series for small phase fluctuations:

$$-E_J \cos \hat{\theta} = -E_J + \frac{E_J}{2} \hat{\theta}^2 - \frac{E_J}{24} \hat{\theta}^4 + \frac{E_J}{720} \hat{\theta}^6 - \dots, \quad (143)$$

where $\hat{\theta} \equiv \hat{\Phi}_J/\varphi_0 = \sum_n \lambda_n (\hat{a}_n + \hat{a}_n^\dagger)$ is the dimensionless phase operator at the junction.

The validity of this expansion requires the phase fluctuations to be small: $\langle \hat{\theta}^2 \rangle \ll 1$. For a transmon in its ground state coupled to a single dominant mode, this condition becomes $\lambda^2(2\bar{n} + 1) \ll 1$ where \bar{n} is the mean photon number. In the vacuum state with $\bar{n} = 0$, the condition reduces to $\lambda^2 \ll 1$, which is the weak-anharmonicity regime characteristic of the transmon. This condition constrains the magnitude of phase fluctuations at the junction, not the strength of bilinear exchange between modes. A device may exhibit large light-matter coupling relative to detunings ($g/|\Delta| \gtrsim 0.1$) while still remaining in the weak-phase-fluctuation regime where the cosine expansion converges.

B. Quadratic Terms: Frequency Renormalization and Bilinear Coupling

The quadratic term in the expansion generates both diagonal (frequency renormalization) and off-diagonal (mode coupling) contributions:

$$\frac{E_J}{2} \hat{\theta}^2 = \frac{E_J}{2} \left(\sum_n \lambda_n (\hat{a}_n + \hat{a}_n^\dagger) \right)^2. \quad (144)$$

Expanding the square separates into diagonal and off-diagonal contributions. The diagonal terms $\sum_n \lambda_n^2 (\hat{a}_n + \hat{a}_n^\dagger)^2$ contribute to mode frequency renormalization. Using the operator identity $(\hat{a} + \hat{a}^\dagger)^2 = \hat{a}^2 + (\hat{a}^\dagger)^2 + 2\hat{a}^\dagger \hat{a} + 1$, the number-conserving term $2\hat{a}_n^\dagger \hat{a}_n$ shifts the mode frequency by $\Delta\omega_n = E_J \lambda_n^2 / \hbar$, while the counter-rotating terms \hat{a}^2 and $(\hat{a}^\dagger)^2$ oscillate rapidly at frequency $2\omega_n$ and average to zero in the rotating-wave approximation.

The off-diagonal terms $E_J \sum_{n < m} \lambda_n \lambda_m (\hat{a}_n + \hat{a}_n^\dagger)(\hat{a}_m + \hat{a}_m^\dagger)$ couple different modes through the Josephson non-linearity. The energy-conserving terms $\hat{a}_n \hat{a}_m^\dagger + \hat{a}_n^\dagger \hat{a}_m$ exchange excitations between modes at rate $g_{nm} = E_J \lambda_n \lambda_m / \hbar$. The counter-rotating terms $\hat{a}_n \hat{a}_m + \hat{a}_n^\dagger \hat{a}_m^\dagger$ create or destroy pairs of excitations, with significant effects only in the ultrastrong coupling regime. The exact Hamiltonian retains all these terms; they are dropped only when making the rotating-wave approximation.

C. Two-Mode Reduction: Qubit and Resonator

For the standard circuit QED setup with a transmon qubit coupled to a readout resonator, we retain

two dominant modes: a qubit-like mode q with large anharmonicity from significant junction participation, and a resonator-like mode r that remains nearly harmonic due to small junction participation. The phase operator reduces to

$$\hat{\theta} = \lambda_q (\hat{b} + \hat{b}^\dagger) + \lambda_r (\hat{a} + \hat{a}^\dagger), \quad (145)$$

where we use \hat{b} for the qubit mode and \hat{a} for the resonator mode to match standard notation.

The quadratic off-diagonal term gives the qubit-resonator interaction:

$$H_{\text{int}}^{(2)} = E_J \lambda_q \lambda_r (\hat{b} + \hat{b}^\dagger)(\hat{a} + \hat{a}^\dagger). \quad (146)$$

This bilinear operator has explicit physical content: it is the coefficient multiplying the full product $(\hat{b} + \hat{b}^\dagger)(\hat{a} + \hat{a}^\dagger)$ in the cosine expansion, containing all four operator products $\hat{b}\hat{a}$, $\hat{b}\hat{a}^\dagger$, $\hat{b}^\dagger\hat{a}$, and $\hat{b}^\dagger\hat{a}^\dagger$. The rotating-wave approximation projects this onto the excitation-exchange sector, but the full bilinear form remains in the exact theory and becomes essential when counter-rotating terms are not negligible.

D. The Rotating-Wave Approximation

In the interaction picture with respect to the free Hamiltonian $H_0 = \hbar\omega_q \hat{b}^\dagger \hat{b} + \hbar\omega_r \hat{a}^\dagger \hat{a}$, the mode operators acquire time dependence: $\hat{a}(t) = \hat{a}(0)e^{-i\omega_r t}$ and $\hat{b}(t) = \hat{b}(0)e^{-i\omega_q t}$. The four terms in the bilinear interaction (146) evolve as

$$\hat{b}\hat{a} \rightarrow e^{-i(\omega_q + \omega_r)t} \hat{b}\hat{a}, \quad (147)$$

$$\hat{b}^\dagger \hat{a}^\dagger \rightarrow e^{+i(\omega_q + \omega_r)t} \hat{b}^\dagger \hat{a}^\dagger, \quad (148)$$

$$\hat{b}^\dagger \hat{a} \rightarrow e^{+i\Delta t} \hat{b}^\dagger \hat{a}, \quad (149)$$

$$\hat{b}\hat{a}^\dagger \rightarrow e^{-i\Delta t} \hat{b}\hat{a}^\dagger, \quad (150)$$

where $\Delta = \omega_q - \omega_r$ is the qubit-resonator detuning.

The first two terms oscillate at the sum frequency $\omega_q + \omega_r$, typically around 10 GHz for superconducting circuits. The last two terms oscillate at the difference frequency $|\Delta|$, typically 0.5–2 GHz in the dispersive regime. When the coupling strength g is much smaller than the sum frequency, the rapidly oscillating terms average to zero over timescales relevant to the dynamics, while the slowly varying terms accumulate significant phase.

The rotating-wave approximation (RWA) retains only the slowly varying terms, giving the Jaynes-Cummings interaction:

$$H_{\text{JC}} = \hbar g (\hat{a}^\dagger \hat{b} + \hat{a} \hat{b}^\dagger), \quad (151)$$

where the coupling constant is identified as

$$g = \frac{E_J \lambda_q \lambda_r}{\hbar} = \frac{E_J}{\hbar} \frac{\phi_q^{J,\text{zpf}} \phi_r^{J,\text{zpf}}}{\varphi_0^2}. \quad (152)$$

This formula has direct physical content: g is proportional to the Josephson energy and to the product of zero-point phase fluctuations at the junction from each mode. In the boundary condition framework, the participation ratios $\phi_q^{J,\text{zpf}}$ and $\phi_r^{J,\text{zpf}}$ are not phenomenological parameters but are computed from the admittance through mode decomposition and normalization. The RWA requires two conditions for validity. First, the coupling must be weak compared to the mode frequencies, $g \ll \omega_q, \omega_r$, ensuring that counter-rotating terms oscillate rapidly relative to the system dynamics. Second, the observation timescale must be long compared to $(\omega_q + \omega_r)^{-1}$, allowing the rapid oscillations to average out.

E. Quartic Terms: The Kerr Nonlinearity

The quartic term in the cosine expansion generates anharmonicity and cross-Kerr interactions:

$$-\frac{E_J}{24}\hat{\theta}^4 = -\frac{E_J}{24}\left(\sum_n \lambda_n(\hat{a}_n + \hat{a}_n^\dagger)\right)^4. \quad (153)$$

Expanding this quartic form and normal-ordering the operators, the leading secular contributions (those that do not oscillate rapidly and average to zero) are the self-Kerr terms proportional to $(\hat{a}_n^\dagger)^2 \hat{a}_n^2$ and the cross-Kerr terms proportional to $\hat{a}_n^\dagger \hat{a}_n \hat{a}_m^\dagger \hat{a}_m$.

The self-Kerr contribution from mode n is

$$H_{\text{self-Kerr}}^{(n)} = -\frac{E_J \lambda_n^4}{4} (\hat{a}_n^\dagger)^2 \hat{a}_n^2 = -\frac{E_J \lambda_n^4}{4} \hat{n}_n (\hat{n}_n - 1), \quad (154)$$

where $\hat{n}_n = \hat{a}_n^\dagger \hat{a}_n$ is the number operator for mode n . This term shifts the energy of the $|n\rangle$ Fock state by $-E_J \lambda_n^4 n(n-1)/4$, creating anharmonicity in the level spacing.

The cross-Kerr contribution between modes n and m is

$$H_{\text{cross-Kerr}}^{(nm)} = -E_J \lambda_n^2 \lambda_m^2 \hat{n}_n \hat{n}_m, \quad (155)$$

which shifts the energy when both modes are excited, creating a photon-number-dependent frequency shift of each mode conditioned on the state of the other.

F. Transmon Anharmonicity

For an isolated transmon qubit (single mode with large junction participation), the self-Kerr term (154) determines the anharmonicity. The energy levels are

$$E_n = \hbar\omega_q n - \frac{E_J \lambda_q^4}{4} n(n-1) + O(\lambda_q^6), \quad (156)$$

where the first term is the harmonic contribution and the second is the leading anharmonic correction.

The anharmonicity, defined as the difference between consecutive transition frequencies, is

$$\alpha \equiv \omega_{12} - \omega_{01} = (E_2 - E_1)/\hbar - (E_1 - E_0)/\hbar = -\frac{E_J \lambda_q^4}{2\hbar}. \quad (157)$$

To connect this to the standard transmon parameter E_C , we use the relationship between the zero-point phase fluctuation and the charging energy. For an isolated transmon in the harmonic approximation, the zero-point phase fluctuation is $\varphi_{\text{zpf}} = (2E_C/E_J)^{1/4}$, where $E_C = e^2/(2C_\Sigma)$ is the charging energy determined by the total capacitance. Identifying $\lambda_q = \varphi_{\text{zpf}}$ gives $\lambda_q^4 = 2E_C/E_J$, and substituting into Eq. (157):

$$\alpha = -\frac{E_C}{\hbar}. \quad (158)$$

This is the well-known result that the transmon anharmonicity equals the charging energy in angular frequency units, with the negative sign indicating that the $|1\rangle \rightarrow |2\rangle$ transition frequency is lower than the $|0\rangle \rightarrow |1\rangle$ transition frequency. The transmon regime $E_J/E_C \gg 1$ corresponds to small anharmonicity $|\alpha| \ll \omega_q$, justifying the perturbative expansion of the cosine.

G. The Dispersive Shift

The dispersive shift arises from second-order perturbation theory in the qubit-resonator coupling. The effective Hamiltonian in the two-mode approximation, combining the results of the previous subsections, is

$$\frac{H}{\hbar} = \omega_r \hat{a}^\dagger \hat{a} + \omega_q \hat{b}^\dagger \hat{b} + \frac{\alpha}{2} \hat{b}^\dagger \hat{b}^\dagger \hat{b} \hat{b} + g(\hat{a}^\dagger \hat{b} + \hat{a} \hat{b}^\dagger), \quad (159)$$

where the RWA has been applied to the coupling term.

In the dispersive regime where $g \ll |\Delta|$ with $\Delta = \omega_q - \omega_r$, the coupling can be treated perturbatively. The unperturbed states are product states $|n_r, n_q\rangle$ with n_r photons in the resonator and n_q excitations in the qubit. The perturbation $V = \hbar g(\hat{a}^\dagger \hat{b} + \hat{a} \hat{b}^\dagger)$ couples states differing by one excitation in each mode.

To second order in perturbation theory, the energy shift of state $|n_r, n_q\rangle$ is

$$E_{n_r, n_q}^{(2)} = \sum_{m_r, m_q \neq n_r, n_q} \frac{|\langle m_r, m_q | V | n_r, n_q \rangle|^2}{E_{n_r, n_q}^{(0)} - E_{m_r, m_q}^{(0)}}. \quad (160)$$

The relevant matrix elements are $\langle n_r + 1, n_q - 1 | V | n_r, n_q \rangle = \hbar g \sqrt{(n_r + 1)n_q}$ for the transition that moves one excitation from qubit to resonator, and $\langle n_r - 1, n_q + 1 | V | n_r, n_q \rangle = \hbar g \sqrt{n_r(n_q + 1)}$ for the reverse process. The energy denominators are $E_{n_r, n_q}^{(0)} - E_{n_r+1, n_q-1}^{(0)} = \hbar(\omega_q - \omega_r) + \hbar\alpha(n_q - 1) = \hbar\Delta + \hbar\alpha(n_q - 1)$ and $E_{n_r, n_q}^{(0)} - E_{n_r-1, n_q+1}^{(0)} = -\hbar\Delta - \hbar\alpha n_q$.

For the ground state $|0, 0\rangle$, only the term with $m_r = 1, m_q = 1$ contributes (via the intermediate state $|1, 1\rangle$)

through second-order virtual processes, but this requires going beyond the linear coupling). The leading contribution to the dispersive physics comes from the states $|0, 0\rangle$, $|1, 0\rangle$, $|0, 1\rangle$, and $|1, 1\rangle$.

Computing the second-order shifts for the states $|0, g\rangle \equiv |0, 0\rangle$, $|1, g\rangle \equiv |1, 0\rangle$, $|0, e\rangle \equiv |0, 1\rangle$, and $|1, e\rangle \equiv |1, 1\rangle$:

For $|0, g\rangle$: no first-order coupling to other states within the low-energy manifold, so $E_{0g}^{(2)} = 0$ to leading order.

For $|1, g\rangle$: couples to $|0, e\rangle$ with matrix element $\hbar g$ and energy denominator $\hbar\omega_r - (\hbar\omega_q) = -\hbar\Delta$. The shift is $E_{1g}^{(2)} = \hbar^2 g^2 / (-\hbar\Delta) = -\hbar g^2 / \Delta$.

For $|0, e\rangle$: couples to $|1, g\rangle$ with matrix element $\hbar g$ and energy denominator $\hbar\omega_q - \hbar\omega_r = \hbar\Delta$. The shift is $E_{0e}^{(2)} = \hbar^2 g^2 / (\hbar\Delta) = \hbar g^2 / \Delta$.

For $|1, e\rangle$: couples to $|0, f\rangle$ (where $|f\rangle$ is the second excited state of the transmon) with matrix element $\hbar g\sqrt{2}$ and energy denominator $\hbar(\omega_q + \alpha) + \hbar\omega_r - 2\hbar\omega_q = \hbar(\omega_r - \omega_q + \alpha) = -\hbar(\Delta - \alpha)$. It also couples to $|2, g\rangle$ with matrix element $\hbar g\sqrt{2}$ and energy denominator $\hbar\omega_q + \hbar\omega_r - 2\hbar\omega_r = \hbar\Delta$. The total shift is $E_{1e}^{(2)} = 2\hbar^2 g^2 / (-\hbar(\Delta - \alpha)) + 2\hbar^2 g^2 / (\hbar\Delta) = -2\hbar g^2 / (\Delta - \alpha) + 2\hbar g^2 / \Delta$.

The dispersive shift χ is defined as the qubit-state-dependent shift of the resonator frequency:

$$\chi = \frac{1}{2} \left[(\omega_r^{|e\rangle}) - \omega_r^{|g\rangle} \right], \quad (161)$$

where $\omega_r^{|g\rangle}$ is the resonator frequency when the qubit is in $|g\rangle$ and $\omega_r^{|e\rangle}$ is the frequency when the qubit is in $|e\rangle$.

From the energy shifts, the resonator frequency in state $|g\rangle$ is $\omega_r^{|g\rangle} = (E_{1g} - E_{0g})/\hbar = \omega_r - g^2/\Delta$. The resonator frequency in state $|e\rangle$ is $\omega_r^{|e\rangle} = (E_{1e} - E_{0e})/\hbar = \omega_r - 2g^2/(\Delta - \alpha) + 2g^2/\Delta - g^2/\Delta = \omega_r + g^2/\Delta - 2g^2/(\Delta - \alpha)$.

The difference is

$$\omega_r^{|e\rangle} - \omega_r^{|g\rangle} = \frac{2g^2}{\Delta} - \frac{2g^2}{\Delta - \alpha} = 2g^2 \left(\frac{\Delta - \alpha - \Delta}{\Delta(\Delta - \alpha)} \right) = \frac{-2g^2\alpha}{\Delta(\Delta - \alpha)}. \quad (162)$$

Using the convention $\chi = (\omega_r^{|e\rangle} - \omega_r^{|g\rangle})/2$ and noting that $\Delta - \alpha = \Delta + |\alpha|$ for $\alpha < 0$:

$$\chi = \frac{g^2\alpha}{\Delta(\Delta + \alpha)}. \quad (163)$$

This is the standard dispersive shift formula. For a transmon with $\alpha < 0$ and qubit frequency below the resonator ($\Delta < 0$), both numerator and denominator are negative products, giving $\chi < 0$: the resonator frequency decreases when the qubit is excited. For qubit frequency above the resonator ($\Delta > 0$), we have $\chi < 0$ when $|\alpha| < \Delta$ (typical operating point) since the numerator is negative and the denominator is positive.

The derivation makes explicit the role of the second transmon level $|f\rangle$ in determining the dispersive

shift. Without the anharmonicity ($\alpha = 0$), the formula would give $\chi = 0$ because the virtual transitions $|1, e\rangle \rightarrow |0, f\rangle$ and $|1, e\rangle \rightarrow |2, g\rangle$ would cancel exactly. The finite anharmonicity breaks this cancellation, producing the nonzero dispersive shift that enables quantum non-demolition readout.

H. Counter-Rotating Corrections

The exact Hamiltonian includes counter-rotating terms that are dropped in the Jaynes-Cummings approximation. The leading correction is the Bloch-Siegert shift, which arises from virtual pair creation and annihilation processes.

In second-order perturbation theory including the counter-rotating terms $\hat{a}\hat{b}$ and $\hat{a}^\dagger\hat{b}^\dagger$, the qubit frequency receives an additional shift:

$$\delta\omega_q^{\text{BS}} = \frac{g^2}{\omega_q + \omega_r}. \quad (164)$$

For typical parameters with $g/2\pi = 100$ MHz and $(\omega_q + \omega_r)/2\pi = 10$ GHz, this shift is approximately 1 MHz—small compared to the qubit frequency but measurable in precision spectroscopy. The ratio $g/(\omega_q + \omega_r) \approx 0.01$ characterizes the validity of the RWA: when this ratio approaches 0.1, the Bloch-Siegert shift becomes significant and the full interaction (146) must be retained.

In the ultrastrong coupling regime where $g/\omega_r \gtrsim 0.1$, counter-rotating processes produce qualitative changes beyond simple frequency shifts: ground state photon population of order $(g/\omega_r)^2$, breakdown of photon number conservation, and failure of the standard input-output relations. The boundary condition framework captures these effects automatically through the full cosine nonlinearity, providing a unified description valid from weak coupling through ultrastrong coupling.

X. DESIGN EXAMPLE: COMPLETE BC FRAMEWORK APPLICATION

This section demonstrates the complete workflow from circuit specification to physical observables, illustrating how the boundary condition framework provides a unified treatment that does not rely on rotating-wave or dispersive approximations at the Hamiltonian level. Different coupling regimes are distinguished by which terms in the cosine expansion are numerically significant, not by changes to the framework itself. Two configurations are analyzed: a dispersive system where perturbative formulas apply and the BC framework validates their accuracy, and a strong-coupling configuration where those formulas fail but the BC framework remains exact.

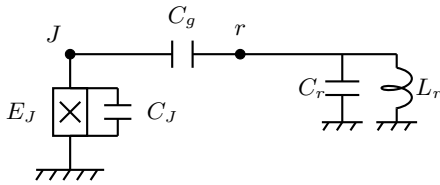


FIG. 10. Transmon qubit at node J capacitively coupled through C_g to a readout resonator represented by its lumped-element equivalent circuit at node r . The junction with Josephson energy E_J is shunted by capacitance C_J ; the resonator is modeled as a parallel LC tank with $\omega_r = 1/\sqrt{L_r C_r}$.

TABLE II. Circuit parameters for the dispersive regime design example.

Component	Symbol	Value	Derived from
Transmon			
	E_J/h	15.0 GHz	Specification
	E_C/h	242 MHz	Specification
	C_J	80 fF	$e^2/(2E_C)$
	L_J	10.90 nH	φ_0^2/E_J
Resonator			
	$\omega_r^{(0)}/2\pi$	7.0 GHz	Specification
	C_r	454.7 fF	$1/(\omega_r Z_0)$
	L_r	1.14 nH	Z_0/ω_r
Coupling			
	C_g	5 fF	Specification
Derived			
	C_Σ	85 fF	$C_J + C_g$
	E_C^{load}/h	228 MHz	$e^2/(2C_\Sigma h)$

A. Dispersive Regime

Consider a transmon qubit capacitively coupled to a coplanar waveguide readout resonator, as shown in Fig. 10. The circuit parameters, summarized in Table II, are chosen to represent a typical dispersive readout configuration.

The Josephson inductance follows from the junction energy as $L_J = \varphi_0^2/E_J = 10.90$ nH, where $\varphi_0 = \Phi_0/2\pi$ is the reduced flux quantum. The resonator, modeled near its fundamental as a lumped LC oscillator with characteristic impedance $Z_0 = 50 \Omega$, has $C_r = 1/(\omega_r^{(0)} Z_0) = 454.7$ fF and $L_r = Z_0/\omega_r^{(0)} = 1.14$ nH.

A critical point often overlooked is that the coupling capacitor C_g contributes to the total shunt capacitance at the junction node. The loaded total capacitance $C_\Sigma = C_J + C_g = 85$ fF yields a loaded charging energy

$$E_C^{\text{load}} = \frac{e^2}{2C_\Sigma} = h \times 228 \text{ MHz}, \quad (165)$$

reduced from the bare value $E_C = h \times 250$ MHz. This distinction proves essential for accurate parameter extraction.

1. Bare and Dressed Frequencies

The bare transmon plasma frequency, computed with the junction capacitance alone, is

$$\omega_p^{\text{bare}} = \sqrt{\frac{8E_J E_C}{\hbar^2}} = 2\pi \times 5.477 \text{ GHz}. \quad (166)$$

However, the physical qubit frequency includes capacitive loading from C_g . Using the loaded charging energy (165), the loaded plasma frequency is

$$\omega_p^{\text{load}} = \sqrt{\frac{8E_J E_C^{\text{load}}}{\hbar^2}} = 2\pi \times 5.229 \text{ GHz}. \quad (167)$$

The 248 MHz downward shift from Eq. (166) to Eq. (167) arises entirely from capacitive loading; hybridization with the resonator provides only a small additional correction in the dispersive regime.

The BC framework determines the dressed mode frequencies by solving the boundary condition equation $sY_{\text{in}}(s) + 1/L_J = 0$, or equivalently by diagonalizing the circuit's capacitance and inductance matrices. The two-node network has capacitance matrix

$$\mathbf{C} = \begin{pmatrix} C_J + C_g & -C_g \\ -C_g & C_r + C_g \end{pmatrix} \quad (168)$$

and inverse inductance matrix $\mathbf{L}^{-1} = \text{diag}(1/L_J, 1/L_r)$. The generalized eigenvalue problem

$$\mathbf{L}^{-1} \phi_n = \omega_n^2 \mathbf{C} \phi_n \quad (169)$$

yields the dressed mode frequencies

$$\frac{\omega_q}{2\pi} = 5.227 \text{ GHz}, \quad \frac{\omega_r}{2\pi} = 6.967 \text{ GHz}. \quad (170)$$

The dressed qubit frequency agrees with the loaded plasma frequency (167) to within 2 MHz (0.04%), confirming that capacitive loading dominates over hybridization in this dispersive configuration. The resonator shifts downward by 33 MHz from its bare value due to back-action from the qubit.

2. Junction Participation and Coupling Strength

The eigenvectors ϕ_n satisfying Eq. (169) are C-orthonormal: $\phi_m^T \mathbf{C} \phi_n = \delta_{mn}$. The first component ϕ_n^J of each eigenvector determines the junction participation of mode n . The zero-point flux at the junction from mode n is

$$\Phi_n^{J,\text{zpf}} = |\phi_n^J| \sqrt{\frac{\hbar}{2\omega_n}}, \quad (171)$$

and the dimensionless participation ratio is $\lambda_n = \Phi_n^{J,\text{zpf}}/\varphi_0$. Numerical evaluation yields

$$\lambda_q = 0.417, \quad \lambda_r = 0.021. \quad (172)$$

The qubit mode has dominant junction participation with $\lambda_q^2 = 0.17$, while the resonator mode has small participation ($\lambda_r^2 = 4.4 \times 10^{-4}$) reflecting its predominantly photonic character.

The qubit-resonator coupling arises from expanding the Josephson potential in the dressed mode basis. The junction phase operator takes the form

$$\hat{\theta} = \frac{\hat{\Phi}_J}{\varphi_0} = \lambda_q(\hat{b} + \hat{b}^\dagger) + \lambda_r(\hat{a} + \hat{a}^\dagger), \quad (173)$$

where \hat{b} and \hat{a} are the annihilation operators for the qubit and resonator modes respectively. Expanding the cosine potential $-E_J \cos \hat{\theta}$ to quadratic order in the mode amplitudes yields the bilinear interaction

$$\hat{H}_{\text{int}} = E_J \lambda_q \lambda_r (\hat{b} + \hat{b}^\dagger)(\hat{a} + \hat{a}^\dagger). \quad (174)$$

In the rotating-wave approximation, this reduces to the Jaynes-Cummings coupling $\hbar g(\hat{a}^\dagger \hat{b} + \hat{a} \hat{b}^\dagger)$ with

$$g = \frac{E_J \lambda_q \lambda_r}{\hbar} = 2\pi \times 131.1 \text{ MHz}. \quad (175)$$

3. Comparison with Standard Formulas

The standard approximate formula for capacitively coupled transmon-resonator systems, derived under the assumptions of weak coupling and non-interacting bare modes, is [2, 13]

$$g_{\text{std}} = \frac{1}{2} \frac{C_g}{\sqrt{C_\Sigma C_r}} \sqrt{\omega_q \omega_r} \left(\frac{E_J}{8E_C^{\text{load}}} \right)^{1/4}. \quad (176)$$

Evaluating with the dressed frequencies and loaded charging energy gives $g_{\text{std}}/2\pi = 130.0$ MHz, differing from the BC result (175) by only 0.8%. This excellent agreement validates both approaches in the dispersive regime.

The small residual discrepancy arises because Eq. (176) assumes the transmon matrix element $\langle e|\hat{n}|g\rangle \approx (E_J/8E_C)^{1/4}$, which receives corrections at finite E_J/E_C , and neglects terms of order $(C_g/C_J)^2$ in the capacitive coupling. The BC framework makes neither approximation.

4. Regime Verification and Dispersive Shift

The detuning between qubit and resonator modes is $\Delta = \omega_q - \omega_r = -2\pi \times 1.740$ GHz. The dimensionless regime parameters are

$$\frac{g}{|\Delta|} = 0.075, \quad \frac{g}{\omega_r} = 0.019. \quad (177)$$

Both ratios satisfy the dispersive criteria $g/|\Delta| < 0.1$ and $g/\omega_r < 0.1$, confirming that the system operates

TABLE III. Dispersive regime: comparison of BC framework and standard formulas.

Parameter	BC	Standard	Deviation
$\omega_q/2\pi$	5.227 GHz	5.229 GHz	0.04%
$\omega_r/2\pi$	6.967 GHz	7.000 GHz	0.5%
$g/2\pi$	131.1 MHz	130.0 MHz	0.8%
$\alpha/2\pi$	-228 MHz	-228 MHz	—
$\chi/2\pi$	-1.14 MHz	-1.14 MHz	< 0.1%

TABLE IV. Parameter comparison between dispersive and strong coupling configurations.

Parameter	Symbol	Dispersive	Strong
Coupling capacitance	C_g	5 fF	15 fF
Bare resonator frequency	$\omega_r^{(0)}/2\pi$	7.0 GHz	5.4 GHz
Total shunt capacitance	C_Σ	85 fF	95 fF
Loaded charging energy	E_C^{load}/h	228 MHz	204 MHz
Loaded plasma frequency	$\omega_p^{\text{load}}/2\pi$	5.229 GHz	4.946 GHz

well within the dispersive regime where perturbative formulas are accurate.

The transmon anharmonicity, computed with the loaded charging energy, is

$$\alpha = -\frac{E_C^{\text{load}}}{\hbar} = -2\pi \times 228 \text{ MHz}. \quad (178)$$

The dispersive shift from second-order perturbation theory is

$$\chi = \frac{g^2 \alpha}{\Delta(\Delta + \alpha)} = -2\pi \times 1.14 \text{ MHz}. \quad (179)$$

The negative sign indicates that the resonator frequency decreases when the qubit is excited, consistent with $\omega_q < \omega_r$ and $\alpha < 0$.

Table III summarizes the comparison between BC framework results and standard formulas. The agreement to better than 1% across all parameters confirms that the dispersive approximation is well justified for this configuration.

B. Strong Coupling Regime

To illustrate the regime where perturbative formulas break down, the circuit is modified to have stronger coupling and smaller detuning. Table IV lists the modified parameters alongside the dispersive case for comparison.

With the larger coupling capacitance $C_g = 15$ fF, the total shunt capacitance increases to $C_\Sigma = 95$ fF, reducing the loaded charging energy to $E_C^{\text{load}}/h = 204$ MHz. The loaded qubit frequency drops to $\omega_p^{\text{load}}/2\pi = 4.946$ GHz, now below the bare resonator frequency of 5.4 GHz.

1. Dressed Mode Structure

Diagonalizing the capacitance and inductance matrices for the strong coupling configuration yields the dressed frequencies

$$\frac{\omega_-}{2\pi} = 4.895 \text{ GHz}, \quad \frac{\omega_+}{2\pi} = 5.399 \text{ GHz}, \quad (180)$$

with a mode splitting of $(\omega_+ - \omega_-)/2\pi = 504$ MHz. The junction participation ratios for the two dressed modes are

$$\lambda_- = 0.380, \quad \lambda_+ = 0.144. \quad (181)$$

Unlike the dispersive case where the qubit mode had $\lambda_q = 0.417$ and the resonator mode had $\lambda_r = 0.021$, here both modes carry substantial junction participation. Neither mode can be identified as predominantly “qubit-like” or “resonator-like”; they are genuinely hybridized polariton states.

2. Ambiguity of the Coupling Constant

In strong coupling, the concept of a single coupling constant g becomes problematic because different physically-motivated definitions yield inconsistent values. Three natural definitions illustrate this ambiguity. The standard formula (176), which describes coupling between bare (uncoupled) modes, gives

$$g_{\text{bare}} = \frac{1}{2} \frac{C_g}{\sqrt{C_\Sigma C_r}} \sqrt{\omega_p^{\text{load}} \omega_r^{(0)}} \left(\frac{E_J}{8E_C^{\text{load}}} \right)^{1/4} = 2\pi \times 285 \text{ MHz}. \quad (182)$$

The Jaynes-Cummings model predicts a relationship between mode splitting and coupling: $(\omega_+ - \omega_-)^2 = \Delta^2 + 4g^2$ where $\Delta = \omega_p^{\text{load}} - \omega_r^{(0)}$. Inverting this relation with the observed splitting gives

$$g_{\text{split}} = \frac{1}{2} \sqrt{(\omega_+ - \omega_-)^2 - \Delta^2} = 2\pi \times 109 \text{ MHz}. \quad (183)$$

The BC framework formula (175), which describes the bilinear coupling between dressed modes, yields

$$g_{\text{dressed}} = \frac{E_J \lambda_- \lambda_+}{\hbar} = 2\pi \times 822 \text{ MHz}. \quad (184)$$

These three values, 285 MHz, 109 MHz, and 822 MHz, differ by factors of 2.6 to 7.5. The disagreement reflects that these formulas measure fundamentally different physical quantities. The standard formula (176) estimates coupling between *bare* (unhybridized) modes, a hypothetical quantity since the physical eigenmodes are strongly mixed. The splitting formula (183) extracts a coupling using the Jaynes-Cummings avoided-crossing relation, which assumes weak hybridization. The BC framework formula computes the *nonlinear interaction between dressed modes*, a well-defined quantity that determines, for example, cross-Kerr shifts between polariton states.

These quantities coincide in the dispersive limit where dressed modes approach bare modes; in strong coupling they diverge because the bare-mode picture breaks down. The BC framework resolves this not by providing “the correct g ” but by replacing g with quantities that remain well-defined: the dressed frequencies ω_\pm , participation ratios λ_\pm , and all matrix elements of the Josephson nonlinearity in the dressed basis.

3. Breakdown of Perturbative Formulas

The bare detuning $\Delta = \omega_p^{\text{load}} - \omega_r^{(0)} = -2\pi \times 454$ MHz yields the regime parameter

$$\frac{g_{\text{bare}}}{|\Delta|} = \frac{285}{454} = 0.63, \quad (185)$$

which exceeds the dispersive threshold of 0.1 by a factor of six. The system is firmly in the strong coupling regime.

Applying the perturbative dispersive shift formula (179) with g_{bare} and the strong-coupling anharmonicity $\alpha = -2\pi \times 204$ MHz gives

$$\chi_{\text{pert}} = \frac{g_{\text{bare}}^2 \alpha}{\Delta(\Delta + \alpha)} = -2\pi \times 57 \text{ MHz}, \quad (186)$$

with $|\chi_{\text{pert}}/\alpha| = 0.28$. While this ratio is less than unity, the 57 MHz shift is comparable to the anharmonicity itself, signaling that higher-order corrections are no longer negligible. More fundamentally, the factor-of-2.6 disagreement between g_{bare} and g_{split} demonstrates that the Jaynes-Cummings model is not internally consistent in this regime.

4. Connection to Classical Microwave Filter Theory

The breakdown of bare-mode descriptions in strong coupling is well established in classical microwave filter theory. For strongly interacting resonator posts in coaxial filters, equivalent circuits based on individual post resonances fail to reliably describe the structure’s behavior; instead, one must work with the electromagnetic eigenmodes satisfying the boundary conditions [59]. Similarity transformations that recover a coupling matrix between “bare” posts yield mathematically correct frequency responses but obscure the underlying physics and fail to predict other observable quantities.

The present quantum circuit analysis exhibits precisely the same structure. When $g/|\Delta|$ exceeds approximately 0.3, coupling constants defined between bare qubit and resonator modes lose physical meaning, different definitions yield different values, and none correctly predicts all observables. The resolution in both classical and quantum contexts is identical: one must work directly with the dressed eigenmodes obtained from the boundary condition framework.

TABLE V. Summary of design examples in dispersive and strong coupling regimes.

Quantity	Dispersive	Strong Coupling
<i>Circuit parameters</i>		
C_g	5 fF	15 fF
$\omega_r^{(0)}/2\pi$	7.0 GHz	5.4 GHz
$\omega_p^{\text{load}}/2\pi$	5.229 GHz	4.946 GHz
<i>BC framework results (exact)</i>		
$\omega_-/2\pi$	5.227 GHz	4.895 GHz
$\omega_+/2\pi$	6.967 GHz	5.399 GHz
λ_-	0.417	0.380
λ_+	0.021	0.144
<i>Regime classification</i>		
$g_{\text{bare}}/ \Delta $	0.075	0.63
Dispersive? ($g/ \Delta < 0.1$)	Yes	No
<i>Perturbative formulas</i>		
g_{BC} vs g_{std}	Agree (0.8%)	Disagree
χ formula reliable?	Yes	No

5. What the BC Framework Provides

Regardless of coupling strength, the BC framework yields well-defined physical quantities: the dressed mode frequencies ω_n from the boundary condition equation, the participation ratios λ_n from mode normalization, and all matrix elements of the Josephson nonlinearity in the dressed basis. These quantities remain meaningful and experimentally accessible even when perturbative parameters like g and χ lose their physical interpretation.

Table V summarizes the key results from both examples, highlighting how the BC framework provides exact results in both regimes while perturbative formulas fail in strong coupling.

In the dispersive regime, the lower-frequency mode (ω_-) is qubit-like with large junction participation ($\lambda_- = 0.417$), while the higher-frequency mode (ω_+) is resonator-like with small participation ($\lambda_+ = 0.021$). The BC framework and standard formulas agree to better than 1%, validating the perturbative approach.

In strong coupling, both modes have significant junction participation ($\lambda_- = 0.380$, $\lambda_+ = 0.144$), indicating substantial hybridization. The modes can no longer be labeled as ‘‘qubit’’ or ‘‘resonator’’; they are polariton states with mixed character. Different definitions of the coupling constant g yield values differing by factors of 2–8, and the dispersive shift formula gives results that are not physically meaningful. The BC framework, however, continues to provide exact dressed frequencies and participation ratios from which all observables can be computed.

C. Design Workflow

The preceding examples establish a systematic workflow for circuit QED design using the BC framework. Beginning with the circuit specification (E_J , E_C , C_J , resonator parameters, coupling elements), one first computes the loaded parameters by accounting for all capacitances shunting the junction node, yielding C_Σ and E_C^{load} . Construction of the capacitance matrix (168) and inverse inductance matrix, followed by solution of the generalized eigenvalue problem (169), provides the dressed mode frequencies and eigenvectors. The junction participation ratios λ_n follow from Eq. (171).

The coupling regime is then identified by evaluating $g_{\text{bare}}/|\Delta|$ using the standard formula (176). For $g/|\Delta| < 0.1$, the dispersive approximation applies: the BC formula (175) agrees with standard expressions to better than 1%, and perturbative formulas for χ and Purcell rates are reliable. For $g/|\Delta| \gtrsim 0.3$, different definitions of g diverge, perturbative formulas become unreliable, and one must extract observables directly from the dressed-mode spectrum provided by the BC framework.

This unified approach, valid from weak to strong coupling, ensures that the quantum description remains anchored to the physical circuit throughout the design process.

XI. DISCUSSION AND CONCLUSIONS

The boundary condition framework developed here builds on three lines of prior work in circuit quantization. Black-box quantization [27] established that the Hamiltonian can be extracted from the electromagnetic admittance without explicit enumeration of environmental modes, and the energy-participation ratio method [32] provided practical computational tools. Multiport impedance quantization [28, 29] developed the mathematical framework for synthesizing positive-real admittance functions as lumped networks, including treatment of ideal transformers and symplectic reduction. The dispersive approximation and its validity conditions have been analyzed extensively [2, 11, 13]. The present work contributes three results that complement this foundation.

The first contribution is the identification of the Schur complement with the eigenvalue-dependent boundary condition at the junction node. Theorem III.2 establishes that the dressed mode frequencies are roots of $sY_{\text{in}}(s) + 1/L_J = 0$, connecting circuit reduction to Sturm-Liouville spectral theory. The second contribution is a theorem-level proof of ultraviolet convergence. Theorem VI.4 shows that under the assumption of finite shunt capacitance, junction participation decays as $\phi_n^J = O(\omega_n^{-1})$ and dimensionless coupling as $\lambda_n = O(\omega_n^{-3/2})$, ensuring absolute convergence of all perturbative sums. This replaces physical arguments

with rigorous bounds. The third contribution is the derivation of standard circuit QED formulas as controlled limits. The coupling strength g , anharmonicity α , and dispersive shift χ emerge from systematic expansion of the exact Hamiltonian, with explicit validity conditions for the rotating-wave and dispersive approximations.

The framework rests on several assumptions that define its scope. The Josephson junction is treated as a lumped element with well-defined phase; spatially extended junctions require distributed treatment. The Josephson energy E_J is constant during the dynamics, so flux-tunable devices are analyzed at fixed bias points. The electromagnetic environment is linear; additional nonlinear elements such as junction arrays or kinetic inductance require extension. Phase fluctuations are as-

sumed moderate with $\langle \hat{\theta}^2 \rangle \lesssim 1$; strong drives populating high-lying states may require numerical treatment of the full cosine potential. Within these assumptions, the exact Hamiltonian (85) provides a foundation for circuit design and analysis that remains anchored to the physical admittance $Y_{\text{in}}(\omega)$ while accommodating electromagnetic environments of arbitrary complexity.

ACKNOWLEDGMENTS

M.B. acknowledges support from EPSRC QT Fellowship grant EP/W027992/1, and EP/Z53318X/1. We thank Smain Amari for useful discussions.

-
- [1] B. D. Josephson, "Possible new effects in superconductive tunnelling," *Phys. Lett.* **1**, 251 (1962).
 - [2] J. Koch *et al.*, "Charge-insensitive qubit design derived from the Cooper pair box," *Phys. Rev. A* **76**, 042319 (2007).
 - [3] A. Parra-Rodriguez, E. Rico, E. Solano, and I. L. Egusquiza, "Quantum networks in divergence-free circuit QED," *Quantum Sci. Technol.* **3**, 024012 (2018).
 - [4] E. Paladino, F. Taddei, G. Giaquinta, and G. Falci, "Josephson nanocircuit in the presence of linear quantum noise," *Physica E* **18**, 39–40 (2003).
 - [5] M. F. Gely, A. Parra-Rodriguez, D. Bothner, Ya. M. Blanter, S. J. Bosman, E. Solano, and G. A. Steele, "Convergence of the multimode quantum Rabi model of circuit quantum electrodynamics," *Phys. Rev. B* **95**, 245115 (2017).
 - [6] E. T. Jaynes and F. W. Cummings, "Comparison of quantum and semiclassical radiation theories with application to the beam maser," *Proc. IEEE* **51**, 89–109 (1963).
 - [7] C. Cohen-Tannoudji, J. Dupont-Roc, and G. Grynberg, *Atom-Photon Interactions: Basic Processes and Applications* (Wiley, New York, 1992).
 - [8] A. Blais *et al.*, "Cavity quantum electrodynamics for superconducting electrical circuits: An architecture for quantum computation," *Phys. Rev. A* **69**, 062320 (2004).
 - [9] A. Wallraff *et al.*, "Strong coupling of a single photon to a superconducting qubit using circuit quantum electrodynamics," *Nature* **431**, 162 (2004).
 - [10] D. I. Schuster *et al.*, "ac Stark shift and dephasing of a superconducting qubit strongly coupled to a cavity field," *Phys. Rev. Lett.* **94**, 123602 (2005).
 - [11] M. Boissonneault, J. M. Gambetta, and A. Blais, "Dispersive regime of circuit QED: Photon-dependent qubit dephasing and relaxation rates," *Phys. Rev. A* **79**, 013819 (2009).
 - [12] A. Frisk Kockum, A. Miranowicz, S. De Liberato, S. Savasta, and F. Nori, "Ultrastrong coupling between light and matter," *Nat. Rev. Phys.* **1**, 19 (2019).
 - [13] A. Blais, A. L. Grimsmo, S. M. Girvin, and A. Wallraff, "Circuit quantum electrodynamics," *Rev. Mod. Phys.* **93**, 025005 (2021).
 - [14] P. A. M. Dirac, "The quantum theory of the emission and absorption of radiation," *Proc. R. Soc. Lond. A* **114**, 243 (1927).
 - [15] E. Fermi, *Nuclear Physics* (University of Chicago Press, Chicago, 1950).
 - [16] E. M. Purcell, "Spontaneous emission probabilities at radio frequencies," *Phys. Rev.* **69**, 681 (1946).
 - [17] A. A. Houck *et al.*, "Controlling the spontaneous emission of a superconducting transmon qubit," *Phys. Rev. Lett.* **101**, 080502 (2008).
 - [18] A. A. Clerk, M. H. Devoret, S. M. Girvin, F. Marquardt, and R. J. Schoelkopf, "Introduction to quantum noise, measurement, and amplification," *Rev. Mod. Phys.* **82**, 1155 (2010).
 - [19] F. Zhang, *The Schur Complement and Its Applications* (Springer, New York, 2005).
 - [20] E. V. Haynsworth, "Determination of the inertia of a partitioned Hermitian matrix," *Linear Algebra Appl.* **1**, 73 (1968).
 - [21] S. Amari, J. Bornemann, and R. Vahldieck, "Accurate analysis of scattering from multiple waveguide discontinuities using the coupled-integral equations technique," *J. Electromagn. Waves Appl.* **10**, 1623 (1996).
 - [22] S. Amari, "Synthesis of cross-coupled resonator filters using an analytical gradient-based optimization technique," *IEEE Trans. Microw. Theory Tech.* **48**, 1559 (2000).
 - [23] C. Turc, Y. Boubendir, and M. Riahi, "Well-conditioned boundary integral equation formulations and Nyström discretizations for the solution of Helmholtz problems with impedance boundary conditions in two-dimensional Lipschitz domains," *J. Comput. Phys.* **342**, 808 (2017).
 - [24] C. Chou, "Domain decomposition algorithms for coupled electromagnetic and circuit simulation," Ph.D. thesis, University of Illinois at Urbana-Champaign (2016).
 - [25] Y. Nakamura, Yu. A. Pashkin, and J. S. Tsai, "Coherent control of macroscopic quantum states in a single-Cooper-pair box," *Nature* **398**, 786–788 (1999).
 - [26] D. I. Schuster *et al.*, "Resolving photon number states in a superconducting circuit," *Nature* **445**, 515 (2007).
 - [27] S. E. Nigg *et al.*, "Black-box superconducting circuit quantization," *Phys. Rev. Lett.* **108**, 240502 (2012).

- [28] F. Solgun, D. W. Abraham, and D. P. DiVincenzo, “Blackbox quantization of superconducting circuits using exact impedance synthesis,” *Phys. Rev. B* **90**, 134504 (2014).
- [29] F. Solgun and D. P. DiVincenzo, “Multiport impedance quantization,” *Ann. Phys.* **361**, 605 (2015).
- [30] A. Parra-Rodriguez, I. L. Egusquiza, D. P. DiVincenzo, and E. Solano, “Canonical circuit quantization with linear nonreciprocal devices,” *Phys. Rev. B* **99**, 014514 (2019).
- [31] U. Vool and M. H. Devoret, “Introduction to quantum electromagnetic circuits,” *Int. J. Circuit Theory Appl.* **45**, 897 (2017).
- [32] Z. K. Mineev *et al.*, “Energy-participation quantization of Josephson circuits,” *npj Quantum Inf.* **7**, 131 (2021).
- [33] Y. Lu *et al.*, “Systematic Construction of Time-Dependent Hamiltonians for Microwave-Driven Josephson Circuits,” arXiv:2512.20743 [quant-ph] (2025).
- [34] I. L. Egusquiza and A. Parra-Rodriguez, “Algebraic canonical quantization of lumped superconducting networks,” *Phys. Rev. B* **106**, 024510 (2022).
- [35] L. Labarca, O. Benhayoune-Khadraoui, A. Blais, and A. Parra-Rodriguez, “Toolbox for nonreciprocal dispersive models in circuit quantum electrodynamics,” *Phys. Rev. Applied* **22**, 034038 (2024).
- [36] M. Alghadeer *et al.*, “Crosstalk Dispersion and Spatial Scaling in Superconducting Qubit Arrays,” arXiv:2512.18148 [quant-ph] (2025).
- [37] C. T. Fulton, “Two-point boundary value problems with eigenvalue parameter contained in the boundary conditions,” *Proc. R. Soc. Edinburgh Sect. A* **77**, 293 (1977).
- [38] J. Walter, “Regular eigenvalue problems with eigenvalue parameter in the boundary condition,” *Math. Z.* **133**, 301 (1973).
- [39] A. Zettl, *Sturm-Liouville Theory* (American Mathematical Society, Providence, RI, 2005).
- [40] P. A. Binding, P. J. Browne, and B. A. Watson, “Sturm–Liouville problems with boundary conditions rationally dependent on the eigenparameter, I,” *Proc. Edinburgh Math. Soc.* **45**(3), 631–645 (2002).
- [41] P. A. Binding, P. J. Browne, and B. A. Watson, “Sturm–Liouville problems with boundary conditions rationally dependent on the eigenparameter, II,” *J. Comput. Appl. Math.* **148**(1), 147–168 (2002).
- [42] A. Dijkstra, H. Langer, and H. S. V. de Snoo, “Symmetric Sturm–Liouville operators with eigenvalue dependent boundary conditions,” in *Canad. Math. Soc. Conf. Proc.* **8**, 87–116 (1987).
- [43] M. Bakr, “A boundary condition perspective on circuit QED dispersive readout,” arXiv:2512.24466 (2025).
- [44] W. E. Lamb and R. C. Retherford, “Fine structure of the hydrogen atom by a microwave method,” *Phys. Rev.* **72**, 241 (1947).
- [45] H. A. Bethe, “The electromagnetic shift of energy levels,” *Phys. Rev.* **72**, 339 (1947).
- [46] R. W. Newcomb, *Linear Multiport Synthesis* (McGraw-Hill, New York, 1966).
- [47] B. D. O. Anderson and S. Vongpanitlerd, *Network Analysis and Synthesis: A Modern Systems Theory Approach* (Prentice-Hall, Englewood Cliffs, NJ, 1973).
- [48] M. H. Devoret, “Quantum fluctuations in electrical circuits,” in *Quantum Fluctuations*, Les Houches Session LXIII, edited by S. Reynaud, E. Giacobino, and J. Zinn-Justin (Elsevier, Amsterdam, 1995), pp. 351–386.
- [49] R. M. Foster, “A reactance theorem,” *Bell Syst. Tech. J.* **3**, 259 (1924).
- [50] O. Brune, “Synthesis of a finite two-terminal network whose driving-point impedance is a prescribed function of frequency,” *J. Math. Phys.* **10**, 191 (1931).
- [51] W. Cauer, *Synthesis of Linear Communication Networks* (McGraw-Hill, New York, 1958).
- [52] B. Gustavsen and A. Semlyen, “Rational approximation of frequency domain responses by vector fitting,” *IEEE Trans. Power Deliv.* **14**, 1052 (1999).
- [53] S. Grivet-Talocia and B. Gustavsen, *Passive Macromodeling: Theory and Applications* (Wiley, 2016).
- [54] A. Parra-Rodriguez and I. L. Egusquiza, “Exact Quantization of Nonreciprocal Quasilumped Electrical Networks,” *Phys. Rev. X* **15**, 011072 (2025).
- [55] M. Bakr *et al.*, “Intrinsic multi-mode interference for passive suppression of Purcell decay in superconducting circuits,” arXiv:2507.09715 (2025).
- [56] M. Bakr *et al.*, “Multiplexed readout of superconducting qubits using a three-dimensional reentrant-cavity filter,” *Phys. Rev. Appl.* **23**, 054089 (2025).
- [57] P. Forn-Díaz *et al.*, “Ultrastrong coupling regimes of light-matter interaction,” *Rev. Mod. Phys.* **91**, 025005 (2019).
- [58] J. Keller *et al.*, “Landau polaritons in highly nonparabolic two-dimensional gases in the ultrastrong coupling regime,” *Phys. Rev. B* **101**, 075301 (2020).
- [59] S. Amari, M. Bakr, and U. Rosenberg, “Properties of building blocks comprising strongly interacting posts and their consideration in advanced coaxial filter designs,” arXiv:2505.15729 (2025).